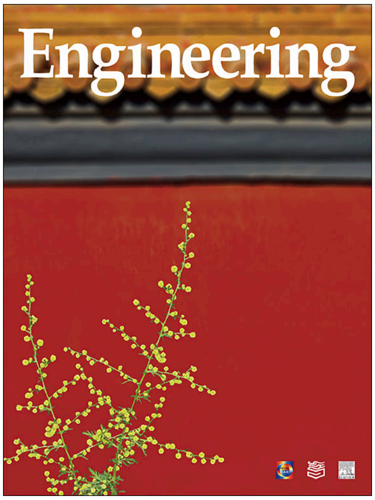

A Stretchable Optogenetic Probe for Wireless Control of Bladder Nociception

Janghoon Joo, Hannah A. Anderson, Wooseok Kim, Shane H. Priester, Bogeun Kim, Firoj Alom, Doyoung Kim, Bhavana Talluri, Hee Kyu Lee, Joohoon Kang, Geumbee Lee, Jae-Young Yoo, Aaron D. Mickle, Sang Min Won

PII: S2095-8099(26)00192-X
DOI: https://doi.org/10.1016/j.eng.2026.03.020
Reference: ENG 2317

To appear in: *Engineering*

Received Date: 6 June 2025
Revised Date: 19 March 2026
Accepted Date: 20 March 2026

Please cite this article as: J. Joo, H.A. Anderson, W. Kim, S.H. Priester, B. Kim, F. Alom, D. Kim, B. Talluri, H.K. Lee, J. Kang, G. Lee, J-Y. Yoo, A.D. Mickle, S.M. Won, A Stretchable Optogenetic Probe for Wireless Control of Bladder Nociception, *Engineering* (2026), doi: https://doi.org/10.1016/j.eng.2026.03.020

Research

Biological Engineering—Article

A Stretchable Optogenetic Probe for Wireless Control of Bladder Nociception

Janghoon Joo [a,#], Hannah A. Anderson [b,c,d,e,#], Wooseok Kim [a], Shane H. Priester [b,c], Bogeun Kim [a], Firoj Alom [b,e], Doyoung Kim [a], Bhavana Talluri [e], Hee Kyu Lee [a], Joohoon Kang [f], Geumbee Lee [g], Jae-Young Yoo [a,h], Aaron D. Mickle [b,c,d,e,i,j,]*, Sang Min Won [a,]*

[a] *Department of Electrical and Computer Engineering, Sungkyunkwan University, Suwon 16419, Republic of Korea*

[b] *Department of Physiological Sciences, College of Veterinary Medicine, University of Florida, Gainesville, FL 32610, USA*

[c] *J. Crayton Pruitt Family Department of Biomedical Engineering, University of Florida, Gainesville, FL 32610, USA*

[d] *Department of Biomedical Engineering, Medical College of Wisconsin, Milwaukee, WI 53226, USA*

[e] *Department of Physiology, Medical College of Wisconsin, Milwaukee, WI 53226, USA*

[f] *Department of Chemical and Biomolecular Engineering, Yonsei University, Seoul 03722, Republic of Korea*

[g] *Department of Chemical Engineering, Kyungpook National University, Daegu 41566, Republic of Korea*

[h] *Department of Semiconductor Convergence Engineering, Sungkyunkwan University, Suwon 16419, Republic of Korea*

[i] *Department of Neurosurgery, Medical College of Wisconsin, Milwaukee, WI 53226, USA*

[j] *Department of Urology, Medical College of Wisconsin, Milwaukee, WI 53226, USA*

* Corresponding authors.

E-mail addresses: amickle@mcw.edu (A.D. Mickle), sangminwon@skku.edu (S.M. Won).

Abstract: Wireless optogenetic systems enable precise manipulation of neural circuits in freely moving animals. However, challenges in accommodating tissue deformation and ensuring stable light delivery limit their application in dynamic organs such as the bladder. Here, we present a fully implantable wireless optogenetic system that addresses these challenges through a bioinspired design, incorporating an intrinsically stretchable polyurethane elastomer tube that encases microscale inorganic light-emitting diodes (μ-ILEDs) and associated electrodes. This design minimizes localized strains and maintains device integrity under cyclic tissue deformation. The system operates at 13.56 MHz via magnetic resonant coupling (MRC) for robust wireless power transfer and programmable light control, ensuring efficient energy harvesting across diverse environments. *In vivo* application in a mouse model of cyclophosphamide (CYP)-induced acute cystitis demonstrated that optogenetic activation of the inhibitory opsin ArchT in TRPV1-lineage sensory neurons modulated nociceptive signaling, as suggested by behavioral changes in a place preference assay. Additionally, the implant did not induce fibrotic encapsulation during the 8-day implantation period, suggesting favorable acute *in vivo* biocompatibility. These findings demonstrate the utility of this system for localized neuromodulation in deformable visceral tissues, with effective *in vivo* validation using a mouse model of bladder nociception.

Keywords: Stretchable optogenetic probe; Wireless bioelectronics; Bladder nociception; Implantable device

1. Introduction

Optogenetics is a technique in neuroscience that enables the manipulation and investigation of neural circuits by selectively activating or inhibiting genetically defined or anatomically restricted neurons through light-sensitive proteins called opsins [1–4]. By introducing these opsins into genetically defined neurons, optogenetics enables fine-tuned control of neuronal activity through light exposure [2,5]. By eliminating the need for direct physical contact between electrodes and neural tissues, optogenetics minimizes tissue damage compared with traditional neuromodulation techniques, such as electrical stimulation methods that require direct contact with tissue [6–8]. Recent advancements in wireless optoelectronics have enhanced the ability to activate opsins expressed in various regions of the nervous system, including the brain [4,9–11], spinal cord [12,13], and peripheral neurons [5,14], in freely moving animals. These wireless technologies enable the modulation of neuronal activity without the constraints of tethered systems, allowing real-time neural control in a more naturalistic and untethered setting.

Despite advancements in wireless platforms, significant challenges remain in achieving effective light delivery to deep tissues and accommodating the dynamic movement of organs such as the bladder. For example, the bladder undergoes repeated cycles of expansion and contraction during normal physiological function, resulting in substantial mechanical deformation of surrounding tissues and implanted structures [5]. Additionally, effective stimulation of neuronal activity within the bladder requires light intensities exceeding 10 $\mathrm{mW \cdot mm^{-2}}$ to penetrate thick tissue layers (> 0.3 mm) while maintaining safe and precise light delivery [14,15].

Existing wireless optogenetic systems, such as the fully internal radio frequency (RF)-powered implants developed by Montgomery et al. [16] and flexible near-field communication (NFC)-based subdermal optoelectronics introduced by Shin et al. [4], represent significant advancements in wireless neural modulation. The former design utilizes a resonant cavity for wireless power transfer, enabling subcutaneous implantation while minimizing tissue heating (< 1 °C) and providing stable optical stimulation across the brain, spinal cord, and peripheral nerves. However, the probe consists of twisted wire pairs encapsulated in an acrylic coating that, while providing structural flexibility, lacks inherent stretchability. Consequently, in dynamic environments such as the bladder—where cyclic volumetric changes induce substantial mechanical deformation of surrounding tissues and implanted structures—this design demonstrates limited mechanical adaptability, potentially leading to structural failure or optical instability during repeated strain cycles. In contrast, the latter design employs ultrathin injectable probes and flexible serpentine interconnects, providing stable subdermal operation even under substantial mechanical deformation (up to 300% stretching). However, owing to the intrinsic nature of the serpentine structures, mechanical stretching results in a non-uniform stress distribution, with significant strain concentration occurring at curvature regions. This localized strain accumulation under repeated deformation can induce structural fatigue and microfractures over time. Although existing designs allow wireless optogenetic delivery in some applications, maintaining structural integrity in environments involving cyclic expansion and contraction—such as in the bladder—remains challenging (Table S1 in Appendix A).

To address these challenges, inspiration can be drawn from nature, where structural designs have evolved to balance mechanical resilience and adaptability. A particularly compelling example is the structural composition of bamboo, whose hollow cylindrical architecture provides resistance to external forces. During growth, bamboo shoots develop into single culms with a natural hollow architecture that allows them to withstand strong winds and heavy loads by dispersing external forces across their surface. This configuration minimizes the transmission of mechanical stress to the interior, offering a model of efficient structural design (Fig. 1(a)) [17,18]. Drawing inspiration from this natural design, we propose a hollow and stretchable cylindrical tube that encases a light-delivery wire within its interior (Fig. 1(b)). This design isolates external strain within the outer tube, effectively shielding the interior wire from mechanical stresses. Consequently, the need for complex serpentine wire geometries to accommodate localized strain is eliminated, simplifying the design while maintaining durability under dynamic conditions. Additionally, the folding mechanism of the tube enables smooth bending of internal components and reduces and evenly distributes mechanical stress along the wire, thereby preserving structural integrity. Finally, bead anchors near the tip provide a fixation strategy within the bladder, limiting device migration without materially altering tube compliance. Integration with a wireless module operating at 13.56 MHz leverages magnetic resonant coupling (MRC) to enable robust and efficient wireless power transfer, facilitating stable light delivery in freely moving animals. This architecture also supports programmable and precise control of optogenetic stimulation, enhancing reliability and flexibility in dynamic biological environments [19–21].

To assess functionality *in vivo*, the devices were implanted within the bladders of freely moving mice subjected to a model of bladder inflammation, and behavioral changes were evaluated for effects suggestive of optogenetic inhibition of nociceptive-lineage neuronal activity. Here, we utilized the inhibitory opsin Archaerhodopsin-3 (Arch), derived from *Halorubrum sodomense* [22], and specifically employed ArchT, a variant from the *Halorubrum* strain TP009 that exhibits more than three-fold higher light sensitivity than traditional Arch [23]. ArchT expression was targeted to transient receptor potential vanilloid 1 (TRPV1)-lineage sensory neurons, which are primarily nociceptive

[24]. Upon activation by green-yellow light (495–590 nm), ArchT hyperpolarizes neurons, thereby inhibiting TRPV1-mediated depolarization. We hypothesized that optogenetic activation of ArchT using our device would suppress TRPV1$^+$ neuronal activity in the bladder and consequently modulate nociceptive signaling in mice subjected to a cyclophosphamide (CYP)-induced model of acute cystitis. The device was implanted directly into the bladder dome, and MRC at 13.56 MHz was applied to activate wireless light delivery. To evaluate the efficacy of neuromodulation by the device, the real-time place preference (RTPP) assay, a modified version of the conditional place preference (CPP) assay, was used to determine whether optogenetic inhibition of the TRPV1-lineage neuronal population is rewarding [14,25–27]. Additionally, histological assessments of the bladder tissue were performed following an 8-day implantation period. Hematoxylin and eosin (H&E), Masson's trichrome, and immunostaining for the pan-leukocyte marker, cluster of differentiation 45 (CD45), were performed to characterize acute host responses. Histological analyses revealed no collagen-rich fibrotic encapsulation and localized CD45$^+$ immune cell recruitment around the probe, indicating a mild foreign-body response during the acute implantation period. The results of the place preference assay, together with these histological assessments, demonstrate that the device is functional *in vivo* and enables localized modulation of peripheral neuronal activity sufficient to influence behavior in freely moving animals while producing minimal host tissue responses during the acute implantation period.

2. Materials and methods

2.1. Fabrication of the wireless power module

The overall device fabrication process is shown in Fig. S1 in Appendix A. Microfabrication of the thin, soft, and flexible wireless power module began by spin-coating polydimethylsiloxane (PDMS, Sylgard 184, Dow, USA) onto a clean glass slide (length × width × thickness = 75 mm × 40 mm × 1 mm) at 500 r·min^{-1} for 30 s. The PDMS layer was then cured at 150 °C for 10 min. Next, a 10 μm-thick copper film was laminated onto the cured PDMS substrate. The copper film was subsequently patterned using an optical fiber laser marker (HY-FMC 20, HYOSUNG Laser, Republic of Korea) to define the desired circuit layout. The circuit layout is fully compatible with standard flexible printed circuit board (PCB) manufacturing processes, enabling scalable production for broader commercial applications (Fig. S2 in Appendix A). After patterning, the unwanted copper regions were removed. Electronic components, including a rectifier (CDBZ0130R-HF), 100 pF capacitor (885012005046, Wurth Elektronik, Germany), and 47 pF capacitor (885012005044, Wurth Elektronik), were then placed at the designated locations on the patterned copper film using conductive paste. Subsequently, 40 American wire gauge (AWG) enamel-coated copper wires (Cu, Remington Industries, USA) were soldered onto the circuit traces to establish electrical connections. The top encapsulation layer was fabricated using PDMS via drop-casting. The final curing process was conducted at 25 °C for 48 h.

2.2. Fabrication of the optoelectronic stimulating component

Two microscale inorganic light-emitting diodes (μ-ILEDs) (SR2130, Cree, USA) were picked up with polyimide tape, placed and aligned on the exposed copper patterns of enamel-coated copper wires, and then firmly secured using solder joints and epoxy (Fig. S3 in Appendix A). The wires were then connected to copper pads at the opposite end to serve as the interconnections between the μ-ILEDs and the wireless power transfer module. The entire μ-ILED probe was then encapsulated within a hollow polyurethane elastomer tube. To enhance the probe stability and protection, both ends of the tube were sealed with epoxy (Loctite Epoxy Marine, Loctite, USA). One end was cured to form a spherical epoxy cap, providing additional structural integrity. Red (HTR650, PhosphorTech Corporation, USA) and yellow (HTY560, PhosphorTech Corporation) phosphors were employed to customize the emission wavelength of the blue μ-ILED (TR2227, Cree). Each phosphor powder was mixed with epoxy 5 min curable epoxy at a 5:1 (phosphor:epoxy) ratio. A small amount of this mixture was applied to the entire surface of each μ-ILED and cured in air for 10 min. The red and yellow phosphors, when excited by the 470 nm emission of the blue μ-ILED, generate red light (peak wavelength = 650 nm) and yellow light (peak wavelength = 630 nm), respectively.

2.3. Light output power measurements

To measure the output power levels of the μ-ILED devices, the current was measured using a digital multimeter (Fluke 179, Fluke Corporation, USA) connected to a separate direct current (DC) power supply (E3631A, Keysight Technologies, USA) during wired operation, while simultaneously positioning the emitting layer above a photodiode power sensor (S121C, Thorlabs, USA) connected to an optical power meter (PM100D, Thorlabs). The output power measured by the light sensor was converted into light intensity by considering the p-n junction area.

2.4. Finite element analysis (FEA) of the copper wire-embedded elastomeric tube

The strain distribution in the copper wire upon bending was modeled using a commercial FEA simulation program, Abaqus (ABAQUS/CAE, Ver. 6.24, Dassault Systemes, France). Symmetric displacement boundary conditions were applied at both ends of the wire to achieve the desired bending radius. In the absence of the elastomeric tube, the wire bent in a folding pattern, whereas in the presence of the elastomeric tube, the bending behavior was determined by the radius of the tube. The copper wire was modeled using hexahedral elements (C3D8R in ABAQUS), and the number of elements was gradually increased until the strain distribution converged, reaching a total of 331 500 elements. The Poisson's ratio for copper (v_{copper}) was set to 0.34.

2.5. Mechanical characterization

To determine the Young's modulus of μ-ILEDs embedded in an elastomeric tube, a force gauge (ESM-303, Mark-10 Corporation, USA) was used through analysis of measured stress–strain curves. The measurements were conducted at a strain rate of 1% per second and a maximum strain of 25% under ambient conditions. The electrical resistance of the device was measured using a digital multimeter (Fig. S4 in Appendix A). In addition to the single-stretch analysis, cyclic mechanical tests were conducted to evaluate long-term durability under physiologically relevant conditions. For the tensile cycling test, the device was repeatedly stretched from 0 to 25% strain for a total of 1000 cycles at a frequency of 0.25 Hz (100 cycles per 400 s), resulting in a total test duration of approximately 4000 s. To further evaluate mechanical resilience under complex deformation, a bending fatigue test was performed by applying a compressive force in the direction opposite to tensile deformation using the same Mark-10 system, inducing repeated bending with a radius of approximately 3 mm for 1000 cycles. Throughout both tests, electrical resistance was continuously monitored in real time using a LabVIEW-controlled digital multimeter (NI-USB 4065, National Instruments, USA) to assess the structural and electrical stability of the encapsulated μ-ILEDs and interconnects.

2.6. Kinetic analysis of water accessibility in optoelectronic devices

The water accessibility of the μ-ILEDs embedded within the elastomeric tube was evaluated using a color-changing indicator, pH paper (Universal indicator paper pH 1–11, DOOSAN Scientific, Republic of Korea), to monitor any water penetration. A color-changing indicator was inserted into the tube, and the tube end was sealed with epoxy (Loctite Epoxy Marine, Loctite) to prevent water ingress. The tube was housed within a PDMS chamber to isolate it from the environment, and a 5 mm diameter hole was created in the PDMS chamber corresponding to the tube end. A droplet of phosphate-buffered saline (PBS, pH 7.2) was applied to the end of the tube, and the color change of the indicator was monitored over time to assess the penetration of PBS into the tube. A control experiment was conducted by placing a color-changing indicator outside the tube and exposing it to PBS droplets (Fig. S5 in Appendix A).

2.7. Wireless power transfer system

The wireless power transfer system, capable of delivering 13.56 MHz signals at an RF output power of up to 10 W, consists of a power distribution controller (A6102-0198, NeuroLux, USA), an antenna impedance matching box (AUT-0150, NeuroLux), and a desktop computer running a custom application. This system utilizes MRC at 13.56 MHz to achieve efficient wireless power transfer. The device antenna is precisely tuned by matching impedances to resonate with the primary antenna (Fig. S6 in Appendix A). The primary antenna is configured in a double-loop structure, which is designed not only for inductive coupling but also for enhancing field uniformity and reducing spatial variations (30%–50%) commonly observed in typical experimental cages [28]. To validate the function of the device, the generated power was transmitted to a 25 cm × 25 cm × 25 cm (length × width × height) cage equipped with a double-loop primary antenna. The angular dependence of power transfer was assessed by measuring the angle between the bottom of the cage and the device using a protractor. The light output power was measured using an optical power meter (PM100D, Thorlabs) equipped with a photodiode power sensor (S121C, Thorlabs) and was normalized to its maximum value at the center of the double-loop antenna (3 cm).

2.8. Thermal characteristics

The surface temperature changes of the entire device, including the coil, rectifier, capacitor, and the μ-ILEDs embedded within the tube, were monitored using an infrared (IR) camera (A655sc, FLIR Systems, USA). The temperature changes of the tube near the light-emitting region of the μ-ILEDs as a function of duty cycle were recorded. Under conditions typically used for optogenetic stimulation (duty cycle below 40%), the temperature of the μ-ILED surface increased by < 1.0 °C.

2.9. Animals

All procedures involving mice and mouse tissues performed in this study were approved by the respective Institutional Animal Care and Use Committees at the University of Florida and the Medical College of Wisconsin and were in strict accordance with the US National Institutes of Health (NIH) *Guide for the Care and Use of Laboratory Animals*. All procedures were performed during the light cycle (06:00–18:00 h). All mice were housed in cohorts of five or fewer on a 12:12 light cycle with ad libitum access to food and water. For the transgenic mouse model, we crossed the Trpv1-cre line (No. 017769, The Jackson Laboratory, USA) [29] with ArchT/eGFP-Ai40 (No. 021188, The Jackson Laboratory, USA) [30]. All experiments were conducted using female mice. All behavioral procedures were performed at the beginning of the light cycle (08:00–13:00 h).

2.10. Surgical procedures

The surgical preparations were performed as described (Fig. S7 and Table S2 in Appendix A). The devices were sterilized with ethylene oxide (ETO) before implantation. Animals were provided with surgical analgesia using Ethiqa XR® (buprenorphine extended-release injectable suspension; stock 1.3 $mg\cdot mL^{-1}$) (86084-100-30, Fidelis Animal Health™, USA) at 3.25 $mg\cdot kg^{-1}$ subcutaneously (SC), Alloxate™ (meloxicam; stock 5 $mg\cdot mL^{-1}$) (21294589, Pivetal®, USA) at 20 $mg\cdot kg^{-1}$ SC, and Bupivacaine Hydrochloride Injection, USP (stock 5 $mg\cdot mL^{-1}$) (71288-726-52, Meitheal Pharmaceuticals Inc., USA) at < 8 $mg\cdot kg^{-1}$ intraperitoneally (IP). A small (1–1.5 cm) incision along the midline in the suprapubic region was made to expose the bladder, and the bulb of the device was implanted directly within the bladder dome with a 5-0 absorbable suture (D303, Pivetal® WebMax™, USA) using the purse-string suturing technique [31]. The muscle was closed with an absorbable suture, and the skin was closed with a 5-0 size non-absorbable suture (668G, ETHILON®, USA). Postoperative care included monitoring body weight and body condition scores daily for 7 days, and additional administration of meloxicam at 20 $mg\cdot kg^{-1}$ SC was provided every 24 h for the first 72 h, while the buprenorphine extended-release injectable suspension lasted for 72 h. Grooming behavior, movement patterns, and wound healing were also monitored qualitatively daily. In rare instances of mild dehiscence, the wound was re-sutured. However, if dehiscence included the muscle layer, the animal was excluded from the study.

2.11. Behavioral assessments

Seven days after device implantation, baseline voiding behavior and place preference were evaluated. After baseline testing (24–48 h), CYP (C0768-1G; Sigma-Aldrich, USA) was administered IP at a single dose of 150 $mg\cdot kg^{-1}$ to induce acute cystitis. Behavioral testing during the cystitis phase was completed within 48 h of CYP injection. All tests were performed between 08:00 and 13:00 h. Device function (Fig. S8 in Appendix A) was monitored before and after each assay using a camera placed beneath the animal cage (Fig. S9 in Appendix A). Void assay boxes were 3D-printed in a hollow cylindrical shape with an inner diameter of 14.5 cm and a height of 11 cm and were placed on 18 cm × 18 cm sheets of chromatography paper for urine collection. Antennas were wired along the exterior of the void assay cages according to the manufacturer-provided protocol using the NeuroLux Smart System [32], and μ-ILED stimulation was delivered at fixed settings (Tx input power = 5 W; constant stimulation), corresponding to a measured light intensity of 7.5 $mW\cdot mm^{-2}$ at the center of the cage. Void assays were conducted under four conditions for each mouse (light-emitting diode (LED)-on, baseline; LED-off, baseline; LED-on, 12–48 h post-CYP; LED-off, 12–48 h post-CYP) for 2 h. After the session, the chromatography paper was imaged under black-light illumination so that the urine spots fluoresced. Images were captured using an iPhone 12 positioned approximately 30 cm above the paper. These images were analyzed using an original MATLAB (MathWorks, USA) code to quantify the volume and number of void spots based on a standard curve, with a minimum void spot threshold of 1 μL. This analysis code is publicly available on GitHub [33]. The void assay was conducted according to standardized recommendations from published guidelines [34]. Place preference was assessed under two conditions (baseline and 12–48 h post-CYP). A plastic place preference box (46.5 cm × 16 cm × 8.5 cm) was used with a 3D-printed divider insertion (0.7 cm thick with a 5.5 cm opening in height), positioned halfway along the length of the box. Inserting the divider allowed distinction between LED-on and LED-off zones while allowing the mice to move freely throughout the box. Antennas were wired along the exterior of the LED-on zone of the place preference assay cage according to the manufacturer-provided protocol using the NeuroLux Smart System [32], and μ-ILED stimulation was delivered using the same settings as above. The place preference assay was performed for 20 min using a wide-angle video camera (B0202, Arducam, China) placed above the assay cage. The time spent in each zone was manually recorded using a stopwatch by Hannah A. Anderson and Shane H. Priester and expressed as a percentage of the total time. Heatmaps were generated in Python using ezTrack [35] in an Anaconda (Conda) environment with $\sigma = 8$ (where σ is the Gaussian filter). Statistical analyses of all behavioral assays were conducted using GraphPad Prism 10 (Dotmatics, USA). Following euthanasia, laparotomies were performed to confirm that the device remained within the bladder for the duration of testing (Fig. S10 in Appendix A).

2.12. Bladder tissue collection and processing

Seven days after surgical implantation of the device, the mice received an IP injection of CYP (150 $mg \cdot kg^{-1}$; $n = 3$ mice) or an equal-volume IP injection of saline ($n = 3$ mice). At 24 h after injection, animals were anesthetized with a ketamine–xylazine cocktail (1.2 $g \cdot kg^{-1}$ ketamine, 17033-100-10, Dechra, UK; xylazine 21295074, Pivetal®; 1:10, IP) and transcardially perfused with cold 0.01 $mol \cdot L^{-1}$ PBS (1× PBS, 4 °C; BP3994, Thermo Fisher Scientific, USA), followed by cold 10% neutral buffered formalin (NBF, 4 °C; 9400, Epredia, USA). The bladders were post-fixed in 10% NBF at 4 °C for 18 h with the device left *in situ*. The devices were then gently explanted from the tissues, and the bladders were transferred to 70% ethanol for 48 h before paraffin embedding. Whole bladders were embedded, lying flat so that 5 µm formalin-fixed, paraffin-embedded (FFPE) longitudinal sections (four sections per animal per histological assessment) captured both the implantation site at the dome and the remainder of the bladder wall extending toward the urethra.

2.13. Masson's trichrome staining and fibrosis quantification

Local fibrosis at the implantation site was assessed using Masson's trichrome staining. Staining was performed using a Masson's Trichrome Stain Kit (ab150686, Abcam, UK). After deparaffinization and rehydration, the tissues were treated with Bouin's solution and then stained sequentially with Weigert's iron hematoxylin (5 min) and Biebrich scarlet/acid fuchsin (15 min). The sections were subsequently differentiated with phosphomolybdic/phosphotungstic acid (10 min) and counterstained with aniline blue (5 min). Sections were rinsed, treated with 1% acetic acid (3 min), dehydrated in alcohol, cleared in xylene, and mounted with DPX (Millipore Sigma, USA). Images were acquired using a 20× objective as stitched full-section composites on a Keyence BZ-X800 microscope (Keyence Corporation, Japan) with identical exposure settings applied across the groups. Semi-automated quantification was performed using Fiji/ImageJ (version 1.54, NIH, USA) with a custom ImageJ macro [36]. The ImageJ Color Deconvolution tool (Masson's trichrome vector) was used to isolate the collagen-rich blue signal, which was thresholded to capture high-intensity signals corresponding to fibrosis. Fibrosis was quantified as the percentage of blue-threshold pixels relative to the total number of red–green–blue (RGB) pixels in two regions: a user-defined circular implantation region and the remainder of the bladder tissue (excluding the implantation region).

2.14. CD45 immunofluorescence (bladder)

The immune cell infiltration associated with CYP treatment and device implantation was assessed using CD45 immunofluorescence. After deparaffinization and rehydration, antigen retrieval was performed in a citrate-based solution (H-3300, Vector Laboratories, USA) at 95 °C for 20 min. The sections were washed and blocked for 1 h in PBS containing 10% normal goat serum (NGS; 006001, Southern Biotech, USA), 0.1% Triton X-100 (Sigma-Aldrich), and 0.01% sodium azide (Sigma-Aldrich). The sections were then incubated overnight at 4 °C with rabbit anti-CD45 antibody (D3F8Q, 1:100; Cell Signaling Technology #70257, USA). Negative control sections were incubated with the primary antibody. After washing, the sections were incubated with Alexa Fluor 647 goat anti-rabbit IgG (Cat# A21244, RRID:AB_2535812, Thermo Fisher Scientific) secondary antibody (1:1000) for 2 h at room temperature (RT), washed, and mounted with Vectashield containing 4′,6-diamidino-2-phenylindole (DAPI) (H-1200, Vector Laboratories). Images were acquired using a 20× objective as stitched full-field composites on a Nikon Ti2 microscope (Nikon Corporation, Japan), with the $CD45^+$ signal detected in the Alexa 647 channel and settings determined based on negative control sections. Semi-automated quantification was conducted in Fiji/ImageJ using a custom ImageJ macro [36], with the following pipeline: For device implantation evaluation, a polygon tool was used to define the implantation region and non-implanted remainder of the tissue region. For CYP model evaluation, a polygon tool was used to define the non-implanted remainder of the tissue region. Within each defined region, four smaller regions of interest (sub-ROIs) of 1500 × 1500 pixels were placed in a semi-automated, iterative manner. ImageJ randomly generated sub-ROI placements within the defined region, and a single user, blinded to the treatment, iterated this placement until the ROIs were well-dispersed and contained minimal lumen space. DAPI was thresholded per individual ROI to account for topographic changes, and CD45 was thresholded uniformly in all ROIs based on the negative control tissue. For both DAPI and CD45, particle size was counted at 50 to infinity $pixels^2$ ($\geq 5\ \mu m^2$). The ratio of $CD45^+$ particles to DAPI particles was calculated to normalize within the sub-ROI for variations in cell dispersion between treatment types.

2.15. H&E staining and lamina propria analysis

The extent of CYP-induced edema, reflected by increased lamina propria thickness, was assessed using H&E staining. Staining was performed using an H&E kit (H-3502, Vector Laboratories) according to the manufacturer's protocol. Deparaffinized sections were stained with hematoxylin for 5 min, rinsed, blued for 10 s, and counterstained with eosin for 3 min. Sections were then dehydrated in alcohol, cleared in xylene, and mounted with DPX (06522; Millipore Sigma, USA). Images were acquired using a 20× objective as stitched full-section composites on a Keyence BZ-X800 microscope with identical exposure settings applied across the groups. Semi-automated quantification was performed using Fiji/ImageJ with a custom ImageJ macro [36]. For each bladder, four measurements per image were recorded to measure the thickness of the lamina propria across the four images (16 measurements per animal). The measurement locations were selected by a single user blinded to treatment to ensure even sampling throughout the tissue. Measurements in pixel units were converted to micrometers by normalizing to the respective image scale bars.

2.16. DRG immunohistochemistry

Dorsal root ganglia (DRGs) were collected to qualitatively confirm TRPV1 expression in a transgenic mouse model. Animals were anesthetized with the same ketamine–xylazine cocktail described in Section 2.12 and transcardially perfused with cold 0.01 $\mathrm{mol\cdot L^{-1}}$ PBS, followed by cold 4% paraformaldehyde (PFA, 4 °C; 19210, Electron Microscopy Sciences, USA). After perfusion, devices were removed and all DRGs were harvested. DRGs were post-fixed in fresh 4% PFA overnight at 4 °C, then washed three times with 1× PBS for 10 min each at RT on a single platform rocking shaker (RS55S-1114, Reliable Scientific, USA). Nonspecific antibody binding was blocked for 2 h at RT with a blocking solution containing 10% NGS and 0.5% Triton X-100 in 1× PBS. Tissues were then incubated for 72 h at RT on the rocking platform in a primary antibody solution containing anti-green fluorescent protein (GFP; Cat# GFP-1020, RRID:AB_10000240, 1:500, Aves Labs, USA) and anti-Tubulin β-3 (TUBB3; Cat# 802001, RRID:AB_2564645, 1:1000, BioLegend, USA) in 2% NGS and 0.5% Triton X-100 in 1× PBS. Anti-GFP was used to amplify native GFP fluorescence, and β-tubulin (β-tub) was used as a neuronal marker. The designated negative control tissue was maintained in 1× PBS for 72 h at RT on a rocking platform without primary antibodies to assess fluorescent background due to secondary antibodies alone. After washing three times with 1× PBS for 30 min each at RT, tissues were incubated for 18–24 h at RT in a secondary antibody solution of goat anti-chicken IgY (H+L) Alexa Fluor™ 555 (Cat# A-21437, RRID:AB_2535858, Thermo Fisher Scientific) and goat anti-rabbit IgG (H+L) cross-adsorbed Alexa Fluor™ 647 (Cat# A21244, RRID:AB_2535812, Thermo Fisher Scientific), each at 1:1500 in 2% NGS and 0.5% Triton X-100 in 1× PBS. The tissues were then washed three times with 1× PBS for 30 min each at RT. Samples were gently placed onto glass slides (12-550-15, Thermo Fisher Scientific), and coverslips (CLS2975246, Sigma-Aldrich) were mounted using approximately 100 μL of Vectashield = vibrance mounting medium (H-1700-10, Vector Laboratories). Images were captured at 40× magnification on a Keyence BZ-X700 fluorescence microscope (Keyence Corporation), with imaging parameters determined using the negative control tissue. Images were processed using a BZ-X Analyzer (version 1.3.1.1, Keyence Corporation) and Fiji/ImageJ software.

3. Results

3.1. Design and mechanical adaptability

The light-delivery needle, consisting of two μ-ILEDs (305 μm × 205 μm × 100 μm) mounted on 40 AWG enamel-coated copper wires, is enclosed within an elastomeric tube with an inner diameter of 0.3 mm and an outer diameter of 0.64 mm (Fig. 1(c) and Figs. S1 and S11 in Appendix A). The μ-ILEDs are securely attached to wires using solder joints and epoxy, ensuring both electrical conductivity and mechanical stability. A bead-shaped structure at the end of the tube (diameter, 0.7 mm) secures the tube within the bladder lumen following surgical insertion, as described in the Experimental section. The μ-ILEDs are oriented along the tubular axis and positioned approximately 0.5 mm away from the bead structure to minimize direct illumination toward the bead. This design ensures that even if the light-delivery module is pulled during or after implantation, the bead effectively anchors the tube within the sutured bladder while maintaining its position.

Light delivery utilizes a power-receiving coil (10 mm diameter, 12 turns, 150 μm spacing and width, 10 μm thickness) that captures energy from an external transmission loop antenna positioned around the animal's cage. Encapsulation of the power coil in a soft polydimethylsiloxane elastomer layer (500 μm thick) enhances the device's lightweight profile (60 mg) and elasticity (Fig. S12 in Appendix A), allowing seamless insertion between the abdominal skin and muscle while minimizing foreign-body reactions (Fig. 1(d)), as demonstrated in previous studies [29,37]. The miniaturized size of the power coil, with a 10 mm diameter and 1.15 mm thickness, provides mechanical flexibility that allows the system to twist and bend without compromising functionality (Figs. 1(e)–(g)), ensuring adaptability to tissue deformation in dynamic biological environments. FEA further supports this adaptability, demonstrating that the power coil can bend to a minimum bending radius of 4 mm. This behavior is primarily attributed to the simplified structure of the copper traces embedded within a soft elastomer in the coil region (Fig. S13 in Appendix A).

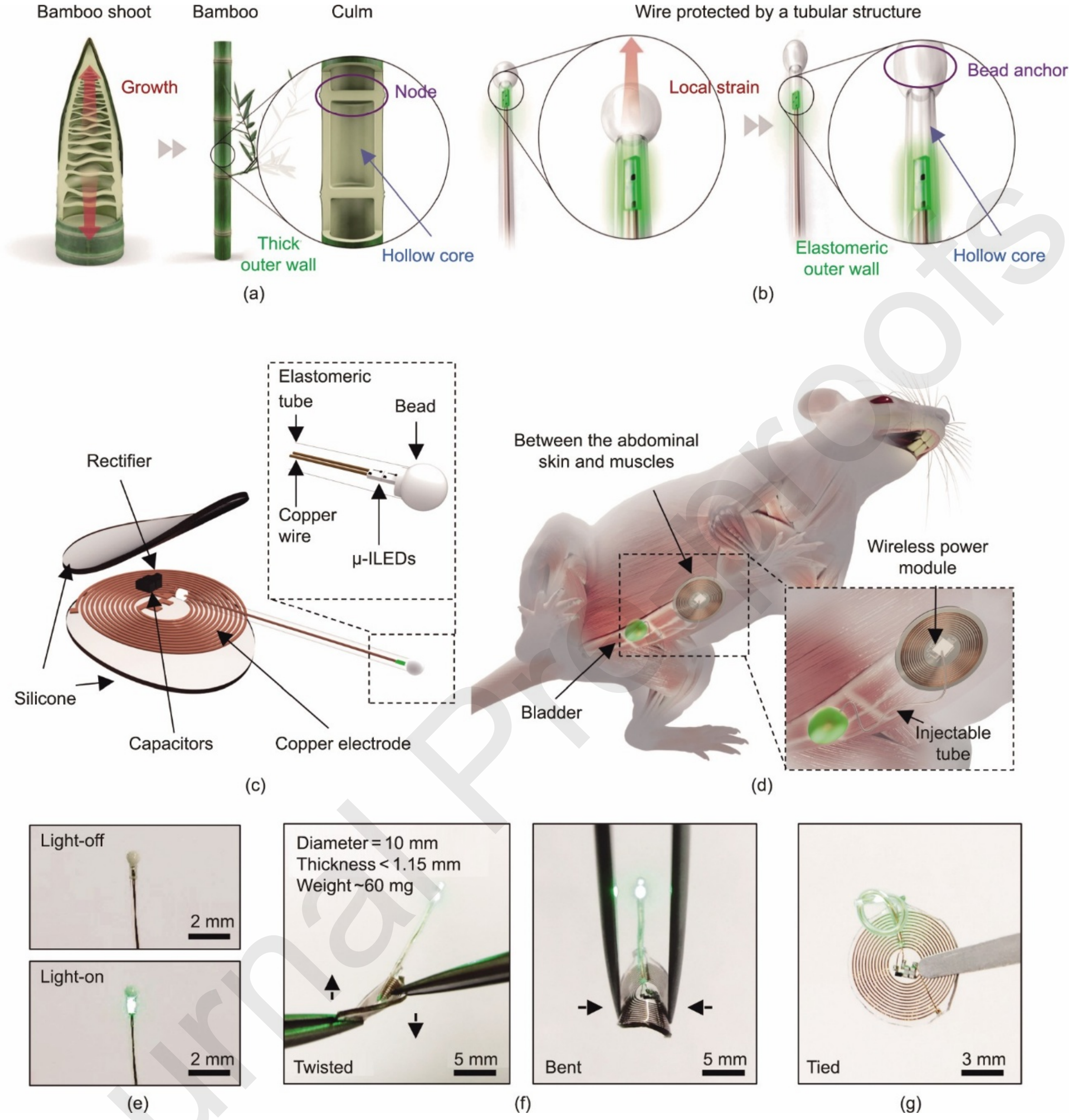

Fig. 1. Design and operational features of tube optoelectronic implants. (a) A schematic illustration and transverse-sectional view of a mature bamboo culm, highlighting the hollow core, thick outer wall, and nodes. (b) A schematic illustration of a hollow tube structure with an inserted wire, designed based on the graded structural inspiration of bamboo. (c) A schematic illustration of the overall wireless optogenetic system. (d) Schematic illustrations showing the positioning of the μ-ILEDs within the bladder, connected through an implanted tube to the receiver coil that is SC implanted anterior to the bladder. (e) Optical images of a tube-enclosed wire connected to μ-ILEDs, showing the light-off condition in the top image and the light-on condition in the bottom image. (f) Photographs of the completed device showing its flexibility under different conditions: (left) twisted and (right) bent. (g) An optical image of the device with the light-delivery needle in a tied condition.

3.2. Optical, mechanical, and long-term stability characteristics

The two μ-ILEDs within the tube deliver optical output intensities exceeding 50 mW·mm^{-2} (Fig. 2(a)), making them suitable for a wide range of optogenetic experiments [38–41]. The transparent tube minimally affects light intensity at lower levels; however, a noticeable reduction occurs at intensities above 80 mW·mm^{-2} due to absorption, scattering, and internal reflection within the tube material (Fig. 2(b)). For example, under high-intensity illumination, polyurethane can exhibit nonlinear optical phenomena such as two-photon absorption, which converts photonic energy into thermal energy, leading to decreased light transmittance [42,43]. Despite these reductions at high intensities, the light intensity required for effective optogenetic stimulation is typically 1 mW·mm^{-2}, as demonstrated in both central and peripheral nervous system tissues [44–46]. Additionally, the μ-ILED features a highly directional emission profile, which inherently limits backward light propagation and reduces optical loss caused by the adjacent bead structure. This behavior is consistent with the stable light intensities observed at lower power levels, as shown in Fig. 2(b). In this study, the μ-ILEDs emit green light at a wavelength of 530 nm to activate ArchT and inhibit TRPV1$^+$ neuronal activity in the bladder of mice. Similar μ-ILED configurations have previously been shown to achieve full-thickness penetration of the bladder wall [47]. In our system, the bead of the device was directly implanted within the bladder dome, thereby minimizing the optical propagation path and associated tissue-induced attenuation. This implantation strategy facilitates efficient and localized light delivery to target neuronal populations. Furthermore, applying a phosphor coating could allow modification of the emitted light color in future prototypes to activate other opsins, such as channelrhodopsin with blue light or halorhodopsin with yellow light, enabling future expansion into different optogenetic applications (Fig. 2(c)).

Enclosing the light-delivery probe within a soft and stretchable tube effectively prevents extreme bending and localized strain caused by the dynamic motion of biological organs after implantation. The tube allows the wire to bend smoothly rather than fold sharply, maintaining a > 0.15 mm bend radius during deformation (Figs. 2(d) and (e)). FEA showed that the maximum strain on the wire inside the tube during folding was 10.9%, which is substantially lower than the 28.2% strain experienced by an exposed wire without the tube. Given that the fracture strain of the copper wire is 29.3% (Fig. S14 in Appendix A), the protective tube design plays a crucial role in preventing wire breakage within the body. Muscular stretching poses a potential risk of wire damage, which is often mitigated using serpentine wire geometries [48,49]. However, under axial tension, serpentine interconnects may localize strain at the curved segments, which have been identified as common sites for fracture initiation and fatigue-induced microcracking. Moreover, solid encapsulation or full bonding/embedding can constrain out-of-plane deformation, thereby increasing the effective strain under a given deformation and reducing elastic stretchability [50,51]. The tube used in this study had a Young's modulus of 9.2 MPa (Fig. S15 in Appendix A), providing an optimal combination of elasticity and flexibility comparable to that of previously reported optogenetic probes [52–54]. Its stretchable properties allow it to elongate during tissue stretching in the abdominal region of a freely moving animal, while keeping the wires and μ-ILEDs inside the tube protected and unstretched, ensuring consistent electrode resistance and stable operation (Fig. 2(f)).

The encapsulating tube structure not only shields the embedded μ-ILEDs and copper wire from acute deformation but also plays a crucial role in sustaining mechanical and electrical performance under physiologically relevant repeated loading. To assess durability under localized mechanical stress, repeated loading comprising 25% axial stretch and repeated bending was applied to emulate bladder distension–relaxation cycles and multiaxial deformations (bending, torsion, and compression) encountered *in vivo* (Figs. S16(a) and (b) in Appendix A). Despite undergoing 1000 cycles of such loading, the probe exhibited negligible changes in electrical resistance, indicating that the copper wire maintained its electrical continuity even under repeated mechanical stress. Importantly, the stress–strain response remained consistent throughout cycling, reflecting the excellent mechanical resilience of the tube and resistance to fatigue-induced softening (Figs. S15 and S16(c) in Appendix A). Notably, prior core–cladding stretchable fiber platforms primarily demonstrated crack suppression and waveguiding stability under high-cycle tensile loading [55–57], whereas our probe maintained stable electrical resistance under repeated bending.

Protection against biofluid penetration is essential to maintain stable functionality of stimulating probes in chronic optogenetic applications [5]. For example, biofluid exposure can cause electrical shorts between electrodes, reduce light intensity, or create direct electrical contact with surrounding tissues, potentially leading to device failure or tissue damage. To evaluate the resistance of the probe to fluid penetration, we performed accelerated soaking in PBS at 70 °C (Fig. S5 in Appendix A). Although 70 °C exceeds physiological temperature, this accelerated soak condition is widely used to probe long-term ingress resistance on compressed timescales. As shown in Fig. 2(g), the probe exhibited no detectable defects or fluid penetration for more than seven days, as indicated by an unchanged pH indicator placed within the tube throughout the test period. We then evaluated the fully integrated wireless system under the same conditions (Fig. S17 in Appendix A). Continuous wireless operation in 70 °C PBS yielded stable optical output without detectable degradation over the test duration, indicating that the assembly maintains integrity during an aggressive soak. These results demonstrate the robust benchtop stability over the tested timescale and support the potential suitability of this encapsulation strategy for long-term optogenetic applications.

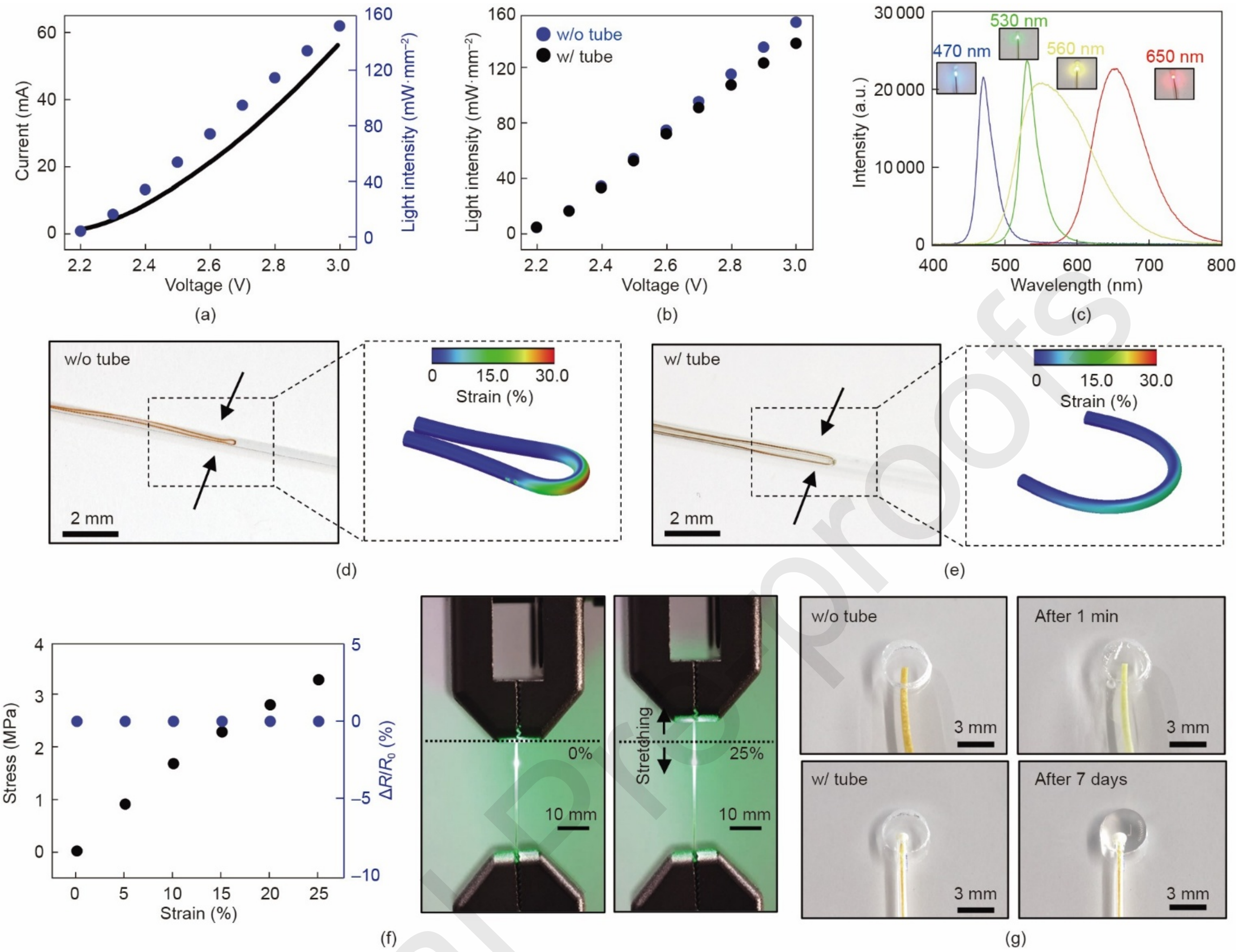

Fig. 2. Electrical, optical, mechanical, and chemical properties of light-delivery needle. (a) Current–voltage–light intensity characteristics. (b) Experimental graph illustrating the variation in μ-ILED light intensity as a function of voltage, with (w/) and without (w/o) the tube. (c) Emission spectra corresponding to the operation of devices constructed with different color μ-ILEDs. (d, e) Images and corresponding finite element modeling results of the wire after folding (d) without a tube and (e) with a tube, respectively. (f) (Left) Experimental graph illustrating the variation of stress and resistance of the wire enclosed within a protective tube as a function of the strain applied to the tube; (right) an optical image demonstrating continuous light illumination even after the tube has been stretched. ΔR: change in resistance; R_0: initial resistance. (g) Experimental comparative images of pH paper with and without a protective tube, captured before and after immersion in PBS solution.

3.3. Wireless optogenetic stimulation

The power coil receives energy through MRC from a transmission loop antenna surrounding the animal cage, and the antenna design is optimized to maximize power transfer efficiency and ensure a uniform magnetic field distribution. Fig. 3(a) illustrates the experimental setup, which consists of a wireless transmitting coil delivering a 13.56 MHz radio-frequency signal with power ranging from 1 to 10 W across a 25 cm × 25 cm area. To further improve power delivery, the transmitting antenna adopts a double-loop configuration with one loop positioned at the bottom of the cage and a second loop surrounding the cage at a height of 5 cm. This configuration enhances the power transfer rate to the device by a factor of five and improves magnetic field uniformity by 44% compared to a single-loop design (Figs. 3(b) and (c)). For example, with an input power of 4 W, the system positioned at the center of the cage, typically the area receiving the least power, achieved a light intensity of 5 $\text{mW}\cdot\text{mm}^{-2}$ at a height of 3 cm from the ground, accounting for scenarios in which the animal hangs from the cage wall or rolls on the floor.

Mechanical bending of the implantable optogenetic system can affect wireless power transmission, resulting in fluctuations in light intensity. The system's output power depends on the magnetic flux (φ) passing through the power-receiving coil, which can be expressed as:

$$\varphi = \iint_S B \cdot \mathrm{d}S \tag{1}$$

where B represents the magnetic field generated by the double-loop transmitting antenna and S denotes the planar area enclosed by the power-receiving coil. When the system bends, the magnetic flux passing through the coil is primarily influenced by changes in the planar area S, assuming that the magnetic field B remains constant. The change in the planar area due to bending can be approximated as:

$$\Delta S = \frac{\left(\frac{d}{R}\right)^2}{32} \tag{2}$$

where d is the inner diameter of the coil and R is the bending radius of curvature. In the coil design used in this study, the inner diameter d was 3.2 mm, and the planar area S decreased by only 0.5% when the curvature radius R was 8 mm. This theoretical prediction aligns with experimental measurements of the optical output at different curvature radii (Fig. 3(d)), which show that the light intensity of the system remains nearly constant for R values greater than 8 mm. Considering that the radius of curvature at the implantation site between the abdominal skin and muscles is typically larger (> 30 mm) [13,14], these findings indicate that the proposed system can maintain reliable operation after implantation.

The light intensity emitted by the system varies with the alignment of the receiving and transmitting coils. Changes in the coil angle affect MRC, reducing the electromotive force induced in the receiving coil and lowering the output power of the system. To evaluate how alignment impacts optical output, the uniformity of the light intensity was measured at different angles, both at the center and edge of the cage, to represent the farthest and closest points to the transmission loop. Fig. 3(e) shows the normalized optical output at a height of 3 cm from the ground, measured across a range of angles, with the input power set to 4 W. The result shows normalized optical output from 1 (5 $\mathrm{mW{\cdot}mm^{-2}}$) to 2.1 at 0°, from 0.7 to 1.6 at 30°, and from 0 to 1.1 at 60°, with measurements taken from the center to the edge of the cage. These findings demonstrate that the system delivers stable optogenetic stimulation across a wide range of animal postures and movements. Although the angular dependence reveals some variability in the center region, this is not a critical limitation of our application. In our targeted case, the device was affixed to the mouse abdominal region, which naturally remained close to the cage surface or walls during movement, and the risk of significant power loss was minimized. Furthermore, the double-loop antenna configuration ensured sufficient field strength in most postures typical of natural movement while maintaining reliable light delivery through optogenetic stimulation.

In addition to angle dependence, the relationship between input power and optical output was assessed. Fig. 3(f) shows that the optical output increased linearly with the input power, both at the center and edge of the cage. As input power increased from 2 to 10 W, the normalized optical output at the center ranged from 0.3 to 2.1, while at the edge it ranged from 1.2 to 4.5, with a normalized output power of 1 corresponding to a light intensity of 5 $\mathrm{mW{\cdot}mm^{-2}}$. This linear relationship allows for precise control of optical output by adjusting the input power to meet the light intensity requirements of different animal models. For example, animal models such as Caenorhabditis elegans, Drosophila larvae, zebrafish, and primates require varying light intensities for effective optogenetic stimulation [59–61]. By fine-tuning input power, the system can achieve the desired levels of light intensity and spatial distribution, ensuring adaptable and precise control over optogenetic experiments.

Thermal damage caused by heat generated from μ-ILEDs is a critical concern in optogenetic systems, as it can result in unintended thermal neural stimulation or tissue injury when implanted *in vivo*. In sensitive organs such as the bladder, elevated temperatures can impair muscle contraction, leading to issues such as incontinence or difficulty in urinating. Therefore, it is crucial for an implanted system to maintain a safe temperature below 38 °C to prevent adverse effects [62]. Fig. 3(g) shows an infrared image of the system's temperature during operation, where the maximum temperature occurs at the μ-ILEDs. Without the protective tube, the system's temperature increases by 2.6 °C above RT (22 °C) after 60 min of operation at a light intensity of 10 $\mathrm{mW{\cdot}mm^{-2}}$ with a 10 Hz pulsed input power. The addition of a protective tube reduces this temperature rise to 2.1 °C, likely due to the insulating effect of the air gap between the μ-ILEDs and the tube. The temperature stabilized after 60 min of operation and remained within a safe range (< 38 °C) for effective optogenetic stimulation (Fig. 3(h)). Notably, the temperature variations were measured relative to RT

(22 °C), and the system showed a negligible temperature change when immersed in PBS at 37 °C, suggesting that the heat generated by the proposed system did not cause damage to the tissues adjacent to the system (Fig. S18 in Appendix A). Although adjusting the duty cycle of the input power can further reduce temperature (Fig. 3(i)), this approach may not be ideal for experiments requiring continuous light stimulation, such as optical inhibition of peripheral neurons. Nevertheless, duty cycle adjustment has been demonstrated to be effective in other optogenetic applications, including noninvasive illumination of cortical layers and regulation of intracellular calcium concentrations [63–65].

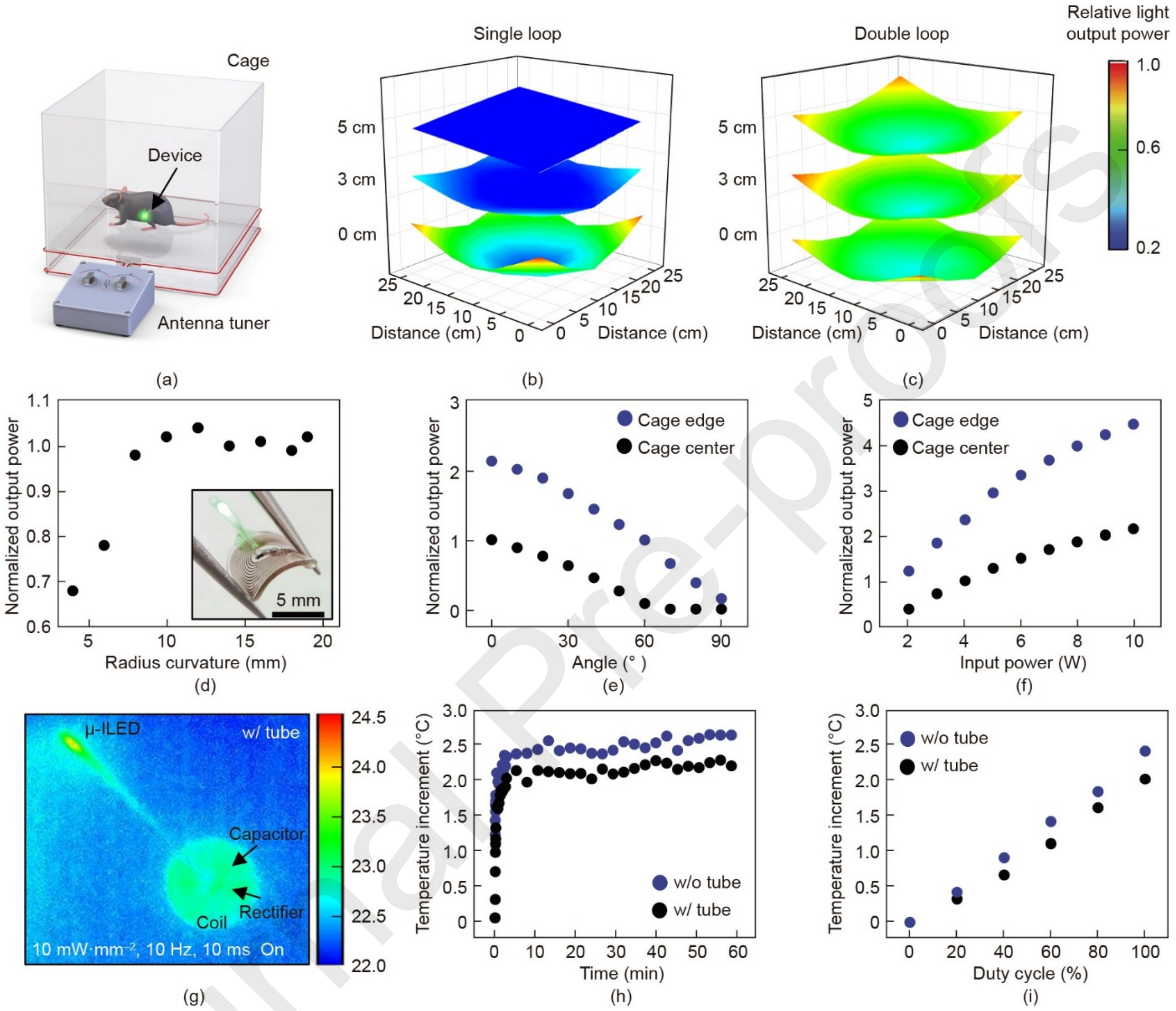

Fig. 3. Power transmission and temperature characteristics of the device operating in the designed double-loop antenna zone. (a) Schematic illustration of the animal cage used to measure the normalized output power. (b, c) Experimental measurement of relative light output power of (b) single-loop and (c) double-loop antenna systems. (d) Normalized optical output as a function of the bending radius of the body of the device. Inset: Photograph showing the device under bending deformation with active μ-ILED illumination. (e, f) Normalized output power as a function of (e) angle variation of the receiving coil at the center and edge of the cage and (f) input power at the center and edge of the cage. (g) IR images of the device surface during wireless operation with a light intensity of 10 mW·mm^{-2} and the pulse parameters of 10 Hz and 100% duty cycle. (h) Graph showing temperature changes of the μ-ILEDs with light intensity of 10 mW·mm^{-2} and the pulse parameters of 10 Hz and 100% duty cycle. (i) Temperature variation around the operating μ-ILEDs as a function of duty cycle of operation with a light intensity of 10 mW·mm^{-2}, with and without tube presence.

3.4. Validation of optogenetic inhibition in a cystitis model

Behavioral evaluations were conducted to assess whether the device effectively elicited optogenetic inhibition of nociceptive TRPV1-lineage neuronal activity in freely moving mice with acute cystitis. The device was implanted in mice expressing the inhibitory opsin ArchT in TRPV1-lineage neurons, as confirmed by immunohistochemistry in the DRG (Fig. S19 in Appendix A). Behavioral assessments, including RTPP and voiding behavior tests, were performed 7–9 days after implantation and before and after induction of CYP-induced cystitis (Fig. 4(a)). Although variability is inevitable in animal behavior assays, the use of RTPP in this study allowed immediate detection of neuronal silencing effects, facilitating efficient observation of pain-associated behaviors. As shown in Figs. 4(b) and (c), activation of the device (measured light intensity = 7.5 $\mathrm{mW \cdot mm^{-2}}$; constant stimulation) drove place preference, with mice spending significantly more time in the μ-ILED-activated chamber following cystitis induction. This statistically significant increase in preference for the powered chamber suggests that the mice experienced some reward from the device-activated chamber. Importantly, preference occurred only after CYP-induced cystitis, supporting device efficacy and consistent with the hypothesis that inhibition of TRPV1-lineage neurons is state-dependent and becomes rewarding only under painful bladder conditions.

Voiding behavior outcomes presented more complex results. As shown in Figs. 4(d)–(f), no statistically significant differences were observed in average void volume or frequency between LED-on and LED-off conditions in the post-CYP group. Rather than reflecting device function, these results can likely be attributed to the complex multifactorial mechanisms involved in bladder voiding, particularly under inflammatory conditions. Although TRPV1-lineage neurons play a known role in bladder nociception, the micturition reflex is mediated by a broader network of sensory and autonomic pathways, including TRPV1-negative neuronal populations [66–68]. Therefore, optogenetic inhibition of $\mathrm{TRPV1^{+}}$ neuronal activity alone may not be sufficient to alleviate voiding dysfunction in CYP-induced cystitis models. Notably, a reduction was observed in voiding frequency under LED-on conditions in the baseline group before CYP-induced cystitis (Fig. 4(f)). This effect suggests that inhibition of TRPV1-lineage neuronal activity can reduce voiding frequency under normal conditions. However, in CYP-induced cystitis, the magnitude of chemically evoked inflammation may exceed the modulatory capacity of optogenetic inhibition in this neuronal population. These results underscore the need for a multimodal approach when interpreting behavioral phenotypes in pain models, as the findings from the place preference assay (Figs. 4(b) and (c)) suggest that device activation is sufficient to modulate behavior.

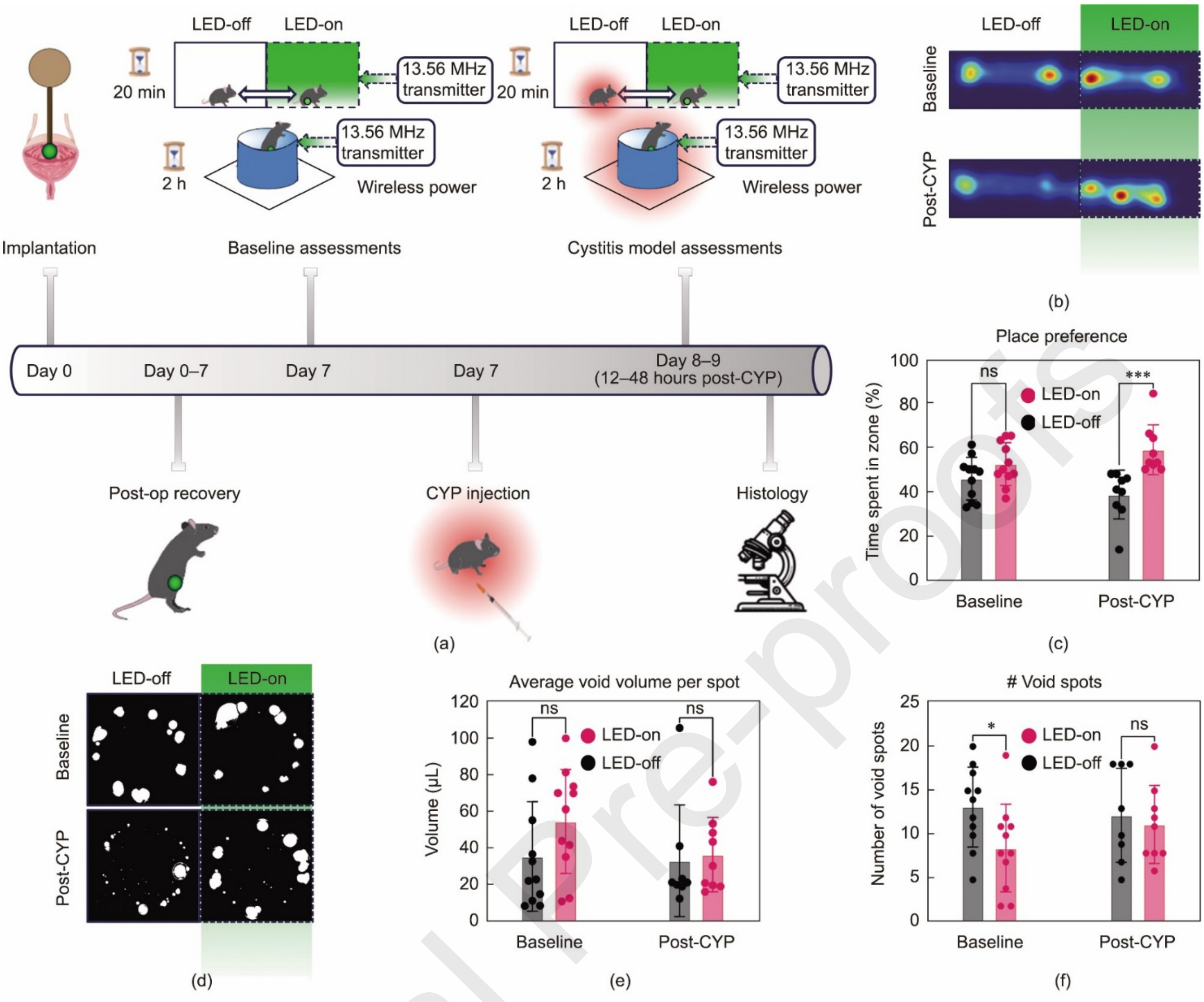

Fig. 4. Validation of the implanted device with behavioral assessments. (a) Timeline of methods, including surgical implantation of the device into the dome of the bladder and subsequent behavioral assessments with and without CYP-induced acute cystitis. (b) Representative heatmaps of baseline and post-CYP place preference assays between LED-off and LED-on chambers from one animal. (c) Data from 20 min baseline and post-CYP place preference assays between LED-off and LED-on chambers. Statistical analysis was conducted by 2-way ANOVA or mixed model, with matching within animals and multiple comparisons between LED treatment status with Šidák correction (baseline: $n = 11$, $p = 0.2623$, post-CYP: $n = 9$, $p = 0.0004$). Mean ± standard deviation (SD) is shown. (d) Representative void blots from 2 h assays from one animal, converted to binary in MATLAB with a 1 μL void spot threshold, as calculated by a standard curve. (e) Average volume per void spot from 2 h void assays, calculated in MATLAB by dividing the total volume by the number of void spots with a 1 μL pixel threshold. Statistical analysis was conducted by 2-way ANOVA or mixed model with matching for within-animal data, with multiple comparisons between LED treatment status with Šidák correction (baseline: $n = 11$, $p = 0.1231$; post-CYP: $n = 9$ LED-on; $n = 8$ LED-off, $p = 0.9992$). Mean ± SD is shown. (f) Void spot frequency of 2 h void assays quantified in MATLAB with a 1 μL void spot threshold. Statistical analysis was conducted by 2-way ANOVA or mixed model with matching for within-animal data, with multiple comparisons between LED treatment status with Šidák correction (baseline: $n = 11$, $p = 0.0121$; post-CYP: $n = 9$ LED-on; $n = 8$ LED-off, $p = 0.5921$). Data are presented as mean ± SD.

3.5. Histological evaluation of device implantation and CYP model

Histological assessments were performed to evaluate the extent of tissue damage caused by the device during the acute implantation period and validate the CYP-induced acute cystitis model. The bladders were collected 1 week after device implantation and 24 h after treatment with saline ($n = 3$) or CYP ($n = 3$). The bladders were processed as longitudinal FFPE sections and stained with Masson’s trichrome, CD45 immunofluorescence, and H&E.

Masson’s trichrome staining was used to assess the fibrotic remodeling in the tissue adjacent to the implantation site (Figs. 5(a) and (b) and Fig. S20 in Appendix A). The percentage of fibrotic area did not differ between the implantation region and the remainder of the tissue when analyzed as per animal means ($n = 6$, paired t-test, $p = 0.3360$) or when all images were treated as independent observations (paired t-test, $p = 0.0717$) (Fig. 5(b)). These data indicate that the polyurethane elastomer tube–μ-ILED probe does not elicit appreciable fibrotic remodeling at the implantation site relative to the remainder of the tissue 8 days after implantation.

The pan-leukocyte marker CD45 was used to evaluate immune cell recruitment to the implantation site (Figs. 5(c) and (d) and Fig. S21 in Appendix A). The mean per-animal ratio of CD45$^+$ particles to DAPI particles (particle size ≥ 50 pixels^2 (≥ 5 μm^2)) across four sub-ROIs per region per four full-section composite images per animal ($n = 6$ animals) was calculated. The CD45/DAPI particle count ratio in the implantation region was significantly higher than that in the rest of the tissue (paired t-test, $p = 0.0009$) (Fig. 5(d)). This quantifies the extent of local immune cell infiltration at the implantation site. Although this is an inevitable component of device implantation *in vivo*, the absence of increased fibrosis in the same region contradicts the formation of a fibrotic capsule within the examined acute window.

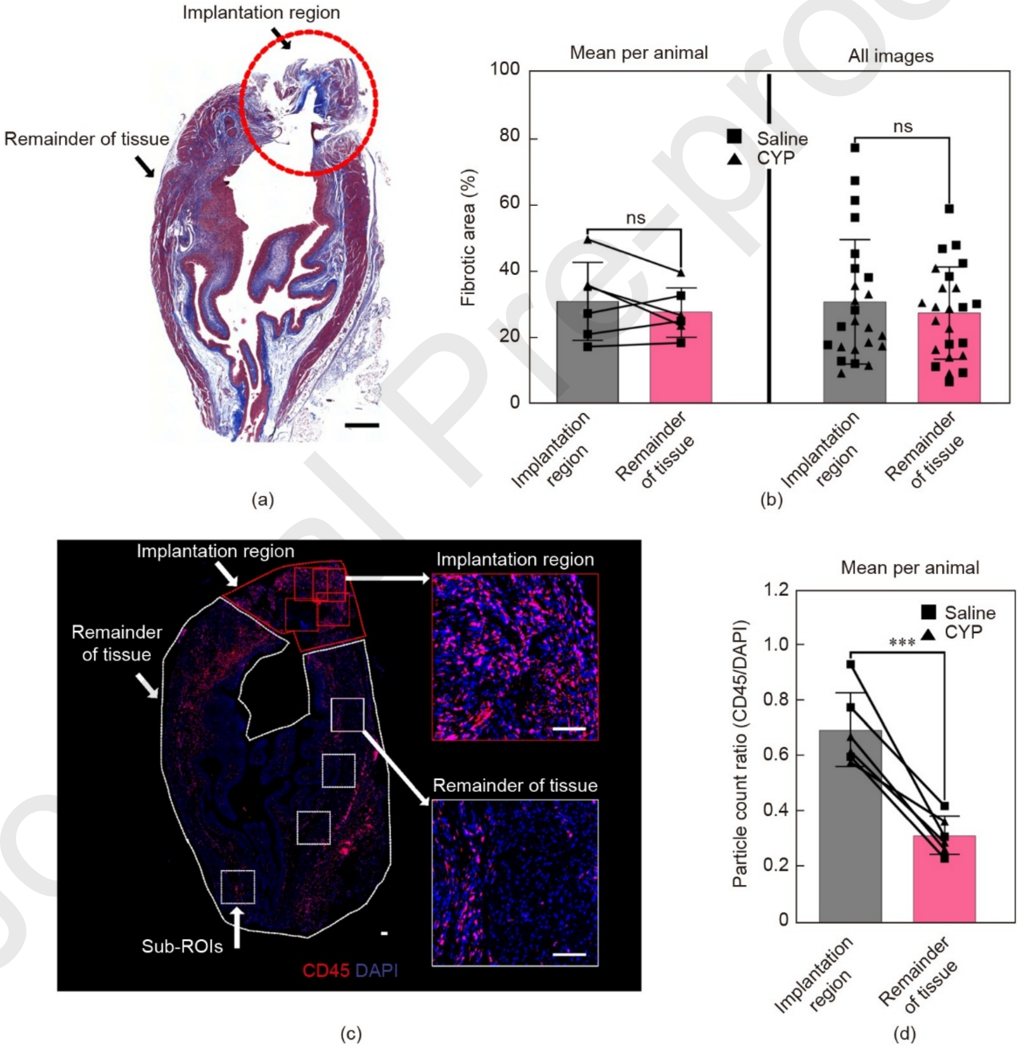

Fig. 5. Histological assessments of bladder tissue regions following device implantation. (a) Representative full-section composite stitched image of a Masson’s trichrome-stained longitudinal bladder section. An oval implantation region was defined (red circle), with the interior labeled “implantation region” and the exterior labeled “remainder of tissue.” Scale bar: 500 μm. (b) Quantification of fibrotic tissue area in bladder regions. Fibrotic tissue area was calculated in the implantation region and the remainder of tissue from full-section composite images as the percentage of blue pixels (defined using the ImageJ Masson’s trichrome color deconvolution tool blue channel) relative to total

RGB pixels. The mean percentage of fibrosis per animal (*n* = 6 animals, 4 images per animal) was not significantly different between the implantation region and the remainder of tissue (left, paired *t*-test, *p* = 0.3360, matching within animal). When individual images were treated as independent observations, there was likewise no difference between regions (right, paired *t*-test, *p* = 0.0717, matching within-image). Data are presented as mean ± SD; ns: not significant, $p > 0.05$. (c) Representative full-section composite stitch image of a CD45 immunofluorescence-stained longitudinal bladder section. Images were acquired with a 20× objective and stitched into full-section composites. A polygon-shaped implantation region was defined (red shape), with the interior labeled "implantation region," and a polygon-shaped non-implantation region was defined, with the interior labeled "remainder of tissue." In each region, 4 smaller regions of interest (sub-ROIs) of 1500 × 1500 pixels were defined. Representative sub-ROI images from each region are shown. CD45 is shown in the red channel, and DAPI is shown in the blue channel. Scale bars: 100 μm. (d) Quantification of $CD45^+$ particles in the Implantation Region and the Remainder of Tissue. The ratio of $CD45^+$ particles (> 50 pixels) to DAPI particles (> 50 pixels) was calculated across 4 sub-ROIs per region per 4 full-section composite images per animal. The mean CD45/DAPI ratio per animal (*n* = 6 animals) was increased in the implantation region (paired *t*-test, ****p* = 0.0009, matching within-animal). Square: saline-treated; triangle: CYP-treated. Data are presented as mean ± SD.

Histological analysis was performed to validate the CYP-induced acute cystitis model. H&E staining was used to measure the lamina propria thickness, an indication of CYP-induced bladder edema, in non-implanted tissue regions (Figs. S22(a) and (b) in Appendix A). Four measurements were recorded for each tissue section, with four tissue sections per animal (*n* = 3 animals per treatment group). The mean lamina propria thickness per animal trended toward an increase in the CYP group compared to the saline group (unpaired *t*-test, *p* = 0.0754) (Fig. S22(b), left). As a supplementary analysis, all measurements were evaluated as independent observations without averaging the replicates within animals. Lamina propria thickness across all individual measurements, treated as independent observations, was significantly higher in the CYP group than in the saline group (unpaired *t*-test, $p < 0.0001$) (Fig. S22(b), right). Although this test did not account for within-animal variability, it demonstrated consistency of the CYP effect. Taken together, the trend toward a significant increase per animal and the significant increase in the group data for lamina propria thickness suggest that CYP induced edema in bladder tissue, consistent with the literature showing similar evaluations at this dosage and time point [69,70].

Immune cell infiltration was evaluated using CD45 immunofluorescence as a pan-leukocyte marker in non-implanted tissue regions (Figs. S22(c) and (d) in Appendix A). The mean per animal was calculated as the ratio of $CD45^+$ particles (> 50 pixels) to DAPI particles (> 50 pixels) across the four sub-ROIs in four full-section composite images per animal (*n* = 3 animals per treatment group). The CD45/DAPI particle count ratio did not differ between CYP and saline groups (unpaired *t*-test, *p* = 0.8213) (Fig. S22(d), left), suggesting that the CYP model induces a mild immune response in the bladder, which is primarily characterized by submucosal edema [71]. Additionally, DAPI-stained nuclei were sparsely distributed upon CYP induction, as indicated by significantly lower mean DAPI particle counts per ROI (unpaired *t*-test, *p* = 0.0031) (Fig. S22(d), right). The sparse cellular distribution supports the idea that the model introduced inflammation and edema to the tissue, consistent with the increased lamina propria thickness observed by H&E staining (Fig. S23 in Appendix A).

Histological evaluation indicated that the device demonstrated acute biocompatibility, with the tissue adjacent to the implantation site showing localized immune cell recruitment but no appreciable fibrotic development within the 8-day implantation period. Additionally, histological analysis suggested that the CYP-induced cystitis model produced structural effects on the bladder tissue at this dosage and time point.

4. Discussion

This study presents a fully implantable wireless optogenetic system that combines robust light delivery with structural resilience, achieved through a protruding geometry and an intrinsically stretchable elastomeric tube. The elastomeric tube encases the μ-ILEDs and their connected electrodes, preventing extreme bending and localized strain caused by the dynamic motion of biological organs. This protective design reduces mechanical stress on sensitive light-emitting components and maintains a stable optical output under repeated bladder filling and emptying. Compared with previously reported wireless μ-ILED devices that use twisted wire pairs or serpentine interconnects [4,13,14], the present system targets hollow, actively deforming viscera and provides enhanced mechanical stability under combined stretch and curvature. Core–cladding stretchable fiber platforms that preserve optical waveguiding under tension offer a complementary strategy [55–57], whereas the current tube-based architecture prioritizes bend-insensitive irradiance rather than waveguiding distance.

In vivo validation in a mouse model of cystitis-associated bladder pain demonstrated that optogenetic activation of ArchT in TRPV1-lineage sensory neurons modulates behavior in a state-dependent manner. Mice showed a significant preference for the LED-on compartment only during CYP-induced cystitis, consistent with an attenuation of nociceptive drive, whereas CYP-phase voiding behavior did not differ between the LED-on and LED-off conditions. While this study supports the notion that TRPV1-lineage inhibition is sufficient to bias the affective, preference-related aspects of bladder pain, it may be insufficient to modulate voiding in the CYP model, where a broader population of C-fiber afferents is recruited during micturition [72]. Histological assessments following an 8-day implantation period supported acute biocompatibility at the device–bladder interface. Evaluation of the device implantation region relative to the remainder of the bladder wall revealed that although a local immune response was observed at the implantation region, no collagen-rich fibrotic capsule formed. These findings indicate a mild, non-fibrotic foreign-body response within the acute window examined. However, future studies with longer implantation periods are necessary to improve understanding of host response.

Several limitations, spanning both device implementation and disease model, frame the scope of the present work. From an engineering standpoint, the current geometry, encapsulation scheme, and 13.56 MHz MRC were optimized for mouse-scale proof-of-concept studies in a 25 cm × 25 cm cage. Translation to larger animals or human-scale bladders will require redesigned transmit and repeater coils, refinement of tube mechanics, and further miniaturization or repartitioning of μ-ILEDs and circuitry. In addition, the overall implant profile may be further reduced by thinning the PDMS overcoat and incorporating ultrathin conformal barriers, such as parylene, in selected regions, which will be evaluated in future iterations. These efforts must be guided by specific absorption rate (SAR) and tissue temperature modeling, as well as appropriate constraints on drive power and duty cycle. Additionally, we evaluated only a single optical stimulation parameter, yielding a binary μ-ILED response; future studies that vary stimulation amplitude, frequency, and duty cycle will be important to establish dose–response relationships and operating safety margins.

Biologically, the experiments were restricted to an acute chemical cystitis model and an acute 8-day implantation period. Evaluation of fibrosis, encapsulation, encrustation, infection risk, and device performance following chronic implantation for weeks to months will guide future studies. The CYP-induced acute cystitis model does not recapitulate complex chronic syndromes such as interstitial cystitis/bladder pain syndrome (IC/BPS), but it replicates chemotherapeutic cystitis. Future studies using disease models that more closely replicate complex diseases will help better illustrate the role of TRPV1-lineage neurons across different disease types. The bladder capacity, compliance, and contractility were not directly measured using cystometry. Instead, the current conclusions rely on behavioral and histological readouts as indirect indicators of gross bladder function preserved during the acute implantation period. Further detailed urological studies are warranted to evaluate the role of TRPV1-lineage neurons in different disease states.

Within these considerations, the tube-encased μ-ILED architecture nevertheless provides a mechanically resilient, wirelessly addressable platform for probing how defined bladder afferent populations contribute to pain-related behaviors in a mechanically active visceral environment. Looking forward, integration of smaller μ-ILEDs via advanced transfer-printing, incorporation of additional opsins and cell types, and scaling of wireless links to larger species could extend this approach toward chronic disease models and, ultimately, translational neuromodulation strategies for deformable hollow organs.

5. Conclusions

This work demonstrates a fully implantable wireless optogenetic system that achieves stable light delivery in a mechanically dynamic visceral organ by combining a protruding μ-ILED probe with an intrinsically stretchable elastomeric tube and a 13.56 MHz MRC link. The tube-based architecture shields the μ-ILEDs and interconnects from extreme bending and localized strain during bladder filling and emptying, providing enhanced mechanical stability compared with previously reported wireless μ-ILED devices. In a CYP-induced acute cystitis model, ArchT-mediated inhibition of TRPV1-lineage sensory neuronal activity altered RTPP without disrupting gross voiding behavior, and complementary histological analyses indicated a mild, non-fibrotic foreign-body response at the device–bladder interface over a one-week implantation period.

These findings position the tube-encased μ-ILED probe as a platform for localized neuromodulation in deformable visceral tissues and for mechanistic studies of bladder nociceptive circuits, while underscoring that further development will be required for direct therapeutic translation. Future work will need to extend these results to chronic cystitis models and longer implantation periods, incorporate additional opsins and cell types, and re-optimize device thickness, emitter dimensions, and wireless coil geometries for larger-animal and human-scale applications.

Acknowledgements

Sang Min Won acknowledge funding from Korea Planning & Evaluation Institute of Industrial Technology (RS-2024-00427006). This work was partly supported by the Institute of Information & Communications Technology Planning & Evaluation (IITP)-ICT Creative Consilience Program grant funded by the Korea government (MSIT) (IITP-2026-RS-2020-II201821). This work was also supported by the National Research Foundation of Korea (NRF) grant funded by the Korean Government (RS-2025-02303342 and RS-2026-25476489). The validation of this device was funded by the Rita Allen Foundation, R21 EB031249, and conducted by the Mickle Lab within the Department of Physiological Sciences, University of Florida, Gainesville, Florida, 32610, USA, and the Department of Physiology, Medical College of Wisconsin, Milwaukee, Wisconsin, 53226, USA.

References

[1] Boyden ES, Zhang F, Bamberg E, Nagel G, Deisseroth K. Millisecond-timescale, genetically targeted optical control of neural activity. Nat Neurosci 2005;8(9):1263–8.

[2] Deisseroth K. Optogenetics Nat Methods 2011;8(1):26–9.

[3] Fenno L, Yizhar O, Deisseroth K. The development and application of optogenetics. Annu Rev Neurosci 2011;34(1):389–412.

[4] Shin G, Gomez AM, Al-Hasani R, Jeong YR, Kim J, Xie Z, et al. Flexible near-field wireless optoelectronics as subdermal implants for broad applications in optogenetics. Neuron 2017;93(3):509–21.e3.

[5] Won SM, Cai L, Gutruf P, Rogers JA. Wireless and battery-free technologies for neuroengineering. Nat Biomed Eng 2023;7(4):405–23.

[6] Rossini PM, Micera S, Benvenuto A, Carpaneto J, Cavallo G, Citi L, et al. Double nerve intraneural interface implant on a human amputee for robotic hand control. Clin Neurophysiol 2010;121(5):777–83.

[7] del Valle J, Navarro X. Interfaces with the peripheral nerve for the control of neuroprostheses. Int Rev Neurobiol 2013;109:63–83.

[8] Kim E, Kim S, Kwon YW, Seo H, Kim M, Chung WG, et al. Electrical stimulation for therapeutic approach. Interdiscip Med 2023;1(2):e20230003.

[9] Carter ME, de Lecea L. Optogenetic investigation of neural circuits *in vivo*. Trends Mol Med 2011;17(4):197–206.

[10] Jeong JW, McCall JG, Shin G, Zhang Y, Al-Hasani R, Kim M, et al. Wireless optofluidic systems for programmable *in vivo* pharmacology and optogenetics. Cell 2015;162(3):662–74.

[11] Lee ST, Williams PA, Braine CE, Lin DT, John SW, Irazoqui PP. A miniature, fiber-coupled, wireless, deep-brain optogenetic stimulator. IEEE Trans Neural Syst Rehabil Eng 2015;23(4):655–64.

[12] Samineni VK, Yoon J, Crawford KE, Jeong YR, McKenzie KC, Shin G, et al. Fully implantable, battery-free wireless optoelectronic devices for spinal optogenetics. Pain 2017;158(11):2108–16.

[13] Kathe C, Michoud F, Schönle P, Rowald A, Brun N, Ravier J, et al. Wireless closed-loop optogenetics across the entire dorsoventral spinal cord in mice. Nat Biotechnol 2022;40(2):198–208.

[14] Samineni VK, Mickle AD, Yoon J, Grajales-Reyes JG, Pullen MY, Crawford KE, et al. Optogenetic silencing of nociceptive primary afferents reduces evoked and ongoing bladder pain. Sci Rep 2017;7(1):15865.

[15] Lv T, Zhong S, Guo X. Establishment of an overactive bladder model in mice. BMC Urol 2023;23(1):19.

[16] Montgomery KL, Yeh AJ, Ho JS, Tsao V, Mohan Iyer S, Grosenick L, et al. Wirelessly powered, fully internal optogenetics for brain, spinal and peripheral circuits in mice. Nat Methods 2015;12(10):969–74.

[17] Liese W. The anatomy of bamboo culms. Beijing: International Network for Bamboo and Rattan (INBAR); 1998.

[18] Nogata F, Takahashi H. Intelligent functionally graded material: bamboo. Compos Eng 1995;5(7):743–51.

[19] Kim J, Banks A, Cheng H, Xie Z, Xu S, Jang KI, et al. Epidermal electronics with advanced capabilities in near-field communication. Small 2015;11(8):906–12.

[20] Yang Y, Wu M, Vázquez-Guardado A, Wegener AJ, Grajales-Reyes JG, Deng Y, et al. Wireless multilateral devices for optogenetic studies of individual and social behaviors. Nat Neurosci 2021;24(7):1035–45.

[21] Yang Y, Wu M, Wegener AJ, Vázquez-Guardado A, Efimov AI, Lie F, et al. Preparation and use of wireless reprogrammable multilateral optogenetic devices for behavioral neuroscience. Nat Protoc 2022;17(4):1073–96.

[22] Chow BY, Han X, Dobry AS, Qian X, Chuong AS, Li M, et al. High-performance genetically targetable optical neural silencing by light-driven proton pumps. Nature 2010;463(7277):98–102.

[23] Han X, Chow BY, Zhou H, Klapoetke NC, Chuong A, Rajimehr R, et al. A high-light sensitivity optical neural silencer: development and application to optogenetic control of non-human primate cortex. Front Syst Neurosci 2011;5:18.

[24] Kwon K, Kim JU, Won SM, Zhao J, Avila R, Wang H, et al. A battery-less wireless implant for the continuous monitoring of vascular pressure, flow rate and temperature. Nat Biomed Eng 2023;7(10):1215–28.

[25] Bimpisidis Z, König N, Wallén-Mackenzie Å. Two different real-time place preference paradigms using optogenetics within the ventral tegmental area of the mouse. J Vis Exp 2020;156:e60867.

[26] McCall JG, Al-Hasani R, Siuda ER, Hong DY, Norris AJ, Ford CP, et al. CRH engagement of the locus coeruleus noradrenergic system mediates stress-induced anxiety. Neuron 2015;87(3):605–20.

[27] Thomas CS, Mohammadkhani A, Rana M, Qiao M, Baimel C, Borgland SL. Optogenetic stimulation of lateral hypothalamic orexin/dynorphin inputs in the ventral tegmental area potentiates mesolimbic dopamine neurotransmission and promotes reward-seeking behaviours. Neuropsychopharmacology 2022;47(3):728–40.

[28] Gutruf P, Krishnamurthi V, Vázquez-Guardado A, Xie Z, Banks A, Su CJ, et al. Fully implantable optoelectronic systems for battery-free, multimodal operation in neuroscience research. Nat Electron 2018;1(12):652–60.

[29] Cavanaugh DJ, Chesler AT, Jackson AC, Sigal YM, Yamanaka H, Grant R, et al. Trpv1 reporter mice reveal highly restricted brain distribution and functional expression in arteriolar smooth muscle cells. J Neurosci 2011;31(13):5067–77.

[30] Maksimovic S, Nakatani M, Baba Y, Nelson AM, Marshall KL, Wellnitz SA, et al. Epidermal Merkel cells are mechanosensory cells that tune mammalian touch receptors. Nature 2014;509(7502):617–21.

[31] Cohen PR, Martinelli PT, Schulze KE, Nelson BR. The purse-string suture revisited: a useful technique for the closure of cutaneous surgical wounds. Int J Dermatol 2007;46(4):341–7.

[32] NeuroLux.org. [Internet]. Northfield: NeuroLux; c2022 [cited 2024 Jul 1]. Available from: http://www.neurolux.org/product-manuals/.

[33] handerson64582. Void-assay-analysis [Internet]. San Francisco: GitHub; c2024 [cited 2024 Jul 1]. Available from: https://github.com/handerson64582/Void-Assay-Analysis.

[34] Hill WG, Zeidel ML, Bjorling DE, Vezina CM. Void spot assay: recommendations on the use of a simple micturition assay for mice. Am J Physiol Renal Physiol 2018;315(5):F1422–9.

[35] Pennington ZT, Dong Z, Feng Y, Vetere LM, Page-Harley L, Shuman T, et al. ezTrack: an open-source video analysis pipeline for the investigation of animal behavior. Sci Rep 2019;9(1):19979.

[36] handerson64582. Green-device-histology-quantification [Internet]. San Francisco: GitHub; c2024 [cited 2025 Dec 1]. Available from: https://github.com/handerson64582/Green-Device-Histology-Quantification.

[37] Grajales-Reyes JG, Copits BA, Lie F, Yu Y, Avila R, Vogt SK, et al. Surgical implantation of wireless, battery-free optoelectronic epidural implants for optogenetic manipulation of spinal cord circuits in mice. Nat Protoc 2021;16(6):3072–88.

[38] Siuda ER, Copits BA, Schmidt MJ, Baird MA, Al-Hasani R, Planer WJ, et al. Spatiotemporal control of opioid signaling and behavior. Neuron 2015;86(4):923–35.

[39] Sparta DR, Stamatakis AM, Phillips JL, Hovelsø N, van Zessen R, Stuber GD. Construction of implantable optical fibers for long-term optogenetic manipulation of neural circuits. Nat Protoc 2012;7(1):12–23.

[40] McCall JG, Kim TI, Shin G, Huang X, Jung YH, Al-Hasani R, et al. Fabrication and application of flexible, multimodal light-emitting devices for wireless optogenetics. Nat Protoc 2013;8(12):2413–28.

[41] Zhang Y, Castro DC, Han Y, Wu Y, Guo H, Weng Z, et al. Battery-free, lightweight, injectable microsystem for *in vivo* wireless pharmacology and optogenetics. Proc Natl Acad Sci USA 2019;116(43):21427–37.

[42] Gao L, Li B, Yi H, Cui J, Yang L, Song Y, et al. Nonlinear optical properties of pyrene derivatives based on a donor-acceptor structure and its polyurethane composites. ACS Omega 2022;7(32):27959–68.

[43] Gao L, Li L, Li B, Yi H, Zhou L, Qu X, et al. Synthesis and nonlinear optical properties of polyurethane composites containing a pyrene derivative. Appl Opt 2023;62(10):2493–500.

[44] Bernstein JG, Boyden ES. Optogenetic tools for analyzing the neural circuits of behavior. Trends Cogn Sci 2011;15(12):592–600.

[45] Emiliani V, Entcheva E, Hedrich R, Hegemann P, Konrad KR, Lüscher C, et al. Optogenetics for light control of biological systems. Nat Rev Methods Prim 2022;2(1):55.

[46] Mattis J, Tye KM, Ferenczi EA, Ramakrishnan C, O'Shea DJ, Prakash R, et al. Principles for applying optogenetic tools derived from direct comparative analysis of microbial opsins. Nat Methods 2012;9(2):159–72.

[47] Mickle AD, Won SM, Noh KN, Yoon J, Meacham KW, Xue Y, et al. A wireless closed-loop system for optogenetic peripheral neuromodulation. Nature 2019;565(7739):361–5.

[48] Zhang Y, Wang S, Li X, Fan JA, Xu S, Song YM, et al. Experimental and theoretical studies of serpentine microstructures bonded to prestrained elastomers for stretchable electronics. Adv Funct Mater 2014;24(14):2028–37.

[49] Kim DH, Liu Z, Kim YS, Wu J, Song J, Kim HS, et al. Optimized structural designs for stretchable silicon integrated circuits. small 2009;5(24):2841–7.

[50] Zhang Y, Xu S, Fu H, Lee J, Su J, Hwang KC, et al. Buckling in serpentine microstructures and applications in elastomer-supported ultra-stretchable electronics with high areal coverage. Soft Matter 2013;9(33):8062–70.

[51] Hu X, Krull P, de Graff B, Dowling K, Rogers JA, Arora WJ. Stretchable inorganic-semiconductor electronic systems. Adv Mater 2011;23(26):2933–6.

[52] Reeder JT, Xie Z, Yang Q, Seo MH, Yan Y, Deng Y, et al. Soft, bioresorbable coolers for reversible conduction block of peripheral nerves. Science 2022;377(6601):109–15.

[53] Jeong YR, Kim J, Xie Z, Xue Y, Won SM, Lee G, et al. A skin-attachable, stretchable integrated system based on liquid GaInSn for wireless human motion monitoring with multi-site sensing capabilities. NPG Asia Mater 2017;9(10):e443.

[54] Song E, Li J, Won SM, Bai W, Rogers JA. Materials for flexible bioelectronic systems as chronic neural interfaces. Nat Mater 2020;19(6):590–603.

[55] Guo J, Liu X, Jiang N, Yetisen AK, Yuk H, Yang C, et al. Highly stretchable, strain sensing hydrogel optical fibers. Adv Mater 2016;28(46):10244–9.

[56] Liu X, Rao S, Chen W, Felix K, Ni J, Sahasrabudhe A, et al. Fatigue-resistant hydrogel optical fibers enable peripheral nerve optogenetics during locomotion. Nat Methods 2023;20(11):1802–9.

[57] Huang S, Liu X, Lin S, Glynn C, Felix K, Sahasrabudhe A, et al. Control of polymers' amorphous-crystalline transition enables miniaturization and multifunctional integration for hydrogel bioelectronics. Nat Commun 2024;15(1):3525.

[58] Zhao Y, Zhou W, Shi Y, Yang X, Bai Y, Li L, et al. Superelastic alloy based electrical interconnects for highly stretchable electronics. npj Flex Electron 2022;6(1):8.

[59] Guo ZV, Hart AC, Ramanathan S. Optical interrogation of neural circuits in Caenorhabditis elegans. Nat Methods 2009;6(12):891–6.

[60] Hwang RY, Zhong L, Xu Y, Johnson T, Zhang F, Deisseroth K, et al. Nociceptive neurons protect Drosophila larvae from parasitoid wasps. Curr Biol 2007;17(24):2105–16.

[61] Douglass AD, Kraves S, Deisseroth K, Schier AF, Engert F. Escape behavior elicited by single, channelrhodopsin-2-evoked spikes in zebrafish somatosensory neurons. Curr Biol 2008;18(15):1133–7.

[62] Sugaya K, de Groat WC. Influence of temperature on activity of the isolated whole bladder preparation of neonatal and adult rats. Am J Physiol Regul Integr Comp Physiol 2000;278(1):R238–46.

[63] Hannanta-anan P, Chow BY. Optogenetic control of calcium oscillation waveform defines NFAT as an integrator of calcium load. Cell Syst 2016;2(4):283–8.

[64] Senova S, Scisniak I, Chiang CC, Doignon I, Palfi S, Chaillet A, et al. Experimental assessment of the safety and potential efficacy of high irradiance photostimulation of brain tissues. Sci Rep 2017;7(1):43997.

[65] Park SI, Brenner DS, Shin G, Morgan CD, Copits BA, Chung HU, et al. Soft, stretchable, fully implantable miniaturized optoelectronic systems for wireless optogenetics. Nat Biotechnol 2015;33(12):1280–6.

[66] DeBerry JJ, Samineni VK, Copits BA, Sullivan CJ, Vogt SK, Albers KM, et al. Differential regulation of bladder pain and voiding function by sensory afferent populations revealed by selective optogenetic activation. Front Integr Nuerosci 2018;12:5.

[67] Forrest SL, Osborne PB, Keast JR. Characterization of bladder sensory neurons in the context of myelination, receptors for pain modulators, and acute responses to bladder inflammation. Front Neurosci 2013;7:206.

[68] Fowler CJ, Griffiths D, de Groat WC. The neural control of micturition. Nat Rev Neurosci 2008;9(6):453–66.

[69] Ni B, Chen Z, Shu L, Shao Y, Huang Y, Tamrat NE, et al. Nrf$_2$ pathway ameliorates bladder dysfunction in cyclophosphamide-induced cystitis via suppression of oxidative stress. Oxid Med Cell Longev 2021;2021(1):4009308.

[70] Kono J, Ueda M, Sengiku A, Suadicani SO, Woo JT, Kobayashi T, et al. Flavonoid nobiletin attenuates cyclophosphamide-induced cystitis in mice through mechanisms that involve inhibition of IL-1β induced connexin 43 upregulation and gap junction communication in urothelial cells. Int J Mol Sci 2022;23(9):5037.

[71] Golubeva AV, Zhdanov AV, Mallel G, Dinan TG, Cryan JF. The mouse cyclophosphamide model of bladder pain syndrome: tissue characterization, immune profiling, and relationship to metabotropic glutamate receptors. Physiol Rep 2014;2(3):e00260.

[72] Saitoh C, Yokoyama H, Chancellor MB, de Groat WC, Yoshimura N. Comparison of voiding function and nociceptive behavior in two rat models of cystitis induced by cyclophosphamide or acetone. Neurourol Urodyn 2010;29(3):501–5.

Declaration of Interest Statement

☒ The authors declare that they have no known competing financial interests or personal relationships that could have appeared to influence the work reported in this paper.

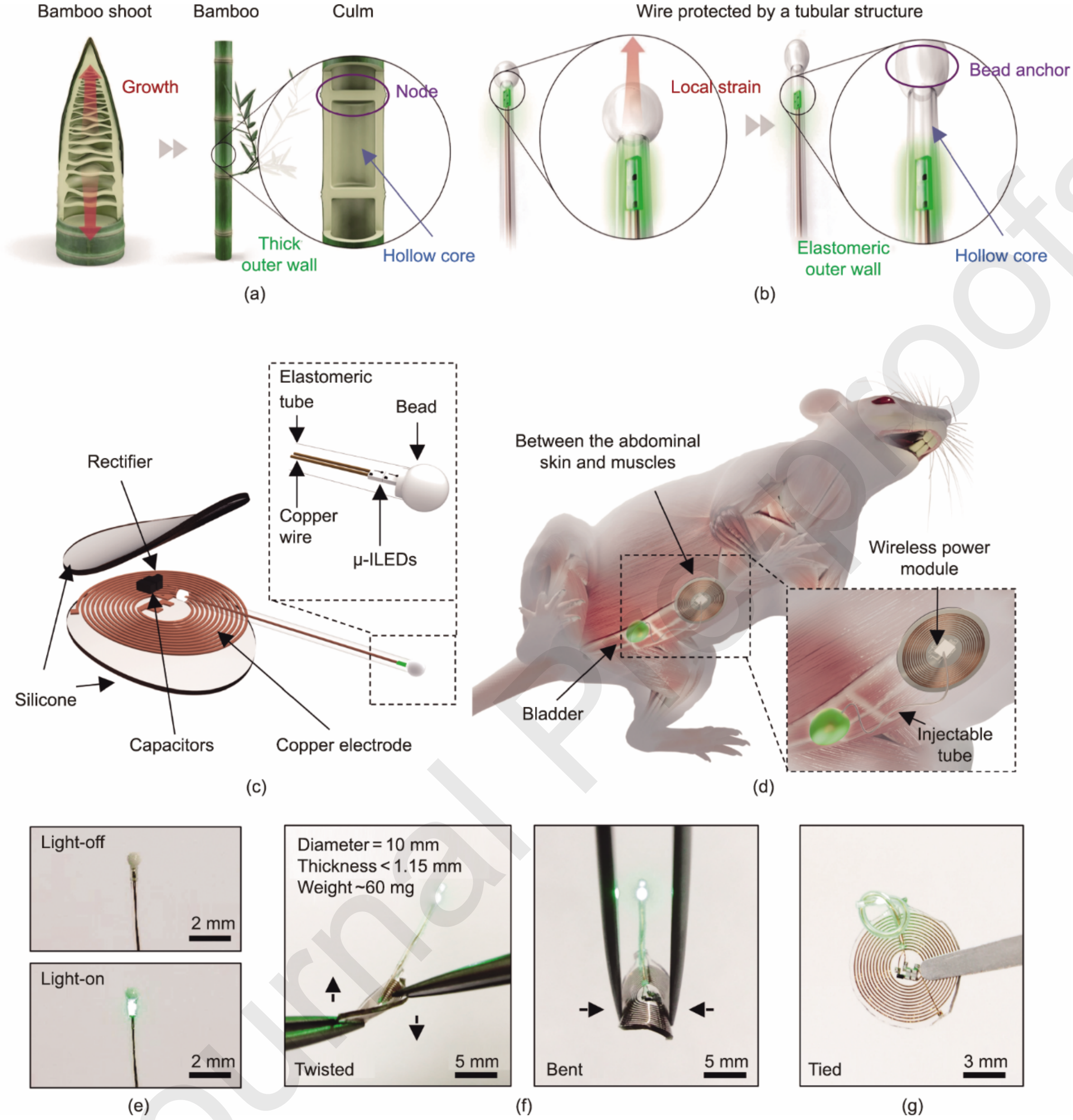
Bamboo shoot
Bamboo
Culm
Growth
Node
Thick
outer wall
Hollow core
(a)
Wire protected by a tubular structure
Local strain
Bead anchor
Elastomeric
outer wall
Hollow core
(b)
Elastomeric
tube
Bead
Copper
wire
μ-ILEDs
Rectifier
Silicone
Capacitors
Copper electrode
(c)
Between the abdominal
skin and muscles
Wireless power
module
Bladder
Injectable
tube
(d)
Light-off
2 mm
Light-on
2 mm
(e)
Diameter = 10 mm
Thickness < 1.15 mm
Weight ~60 mg
Twisted
5 mm
Bent
5 mm
(f)
Tied
3 mm
(g)

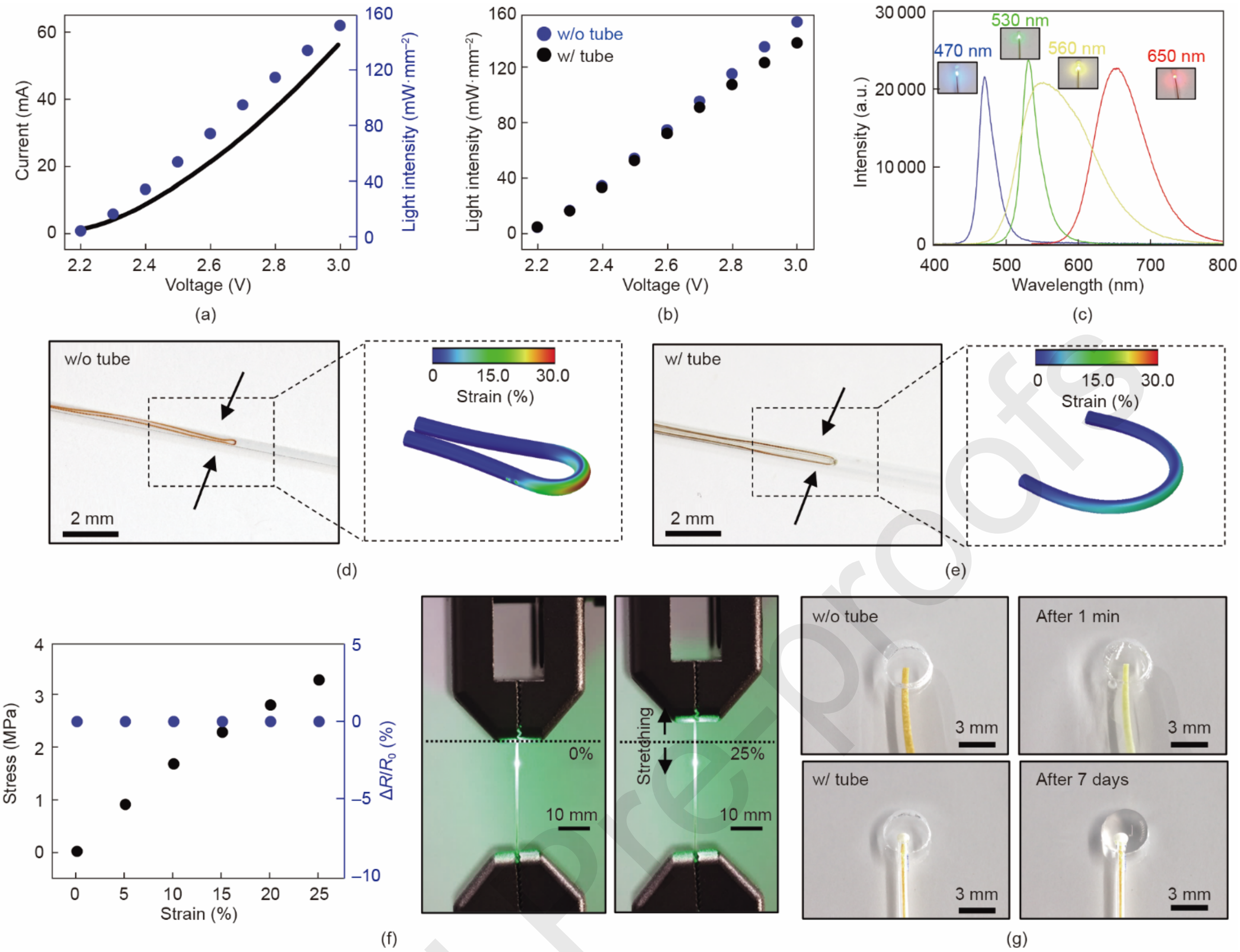
Current (mA)
Light intensity (mW·mm⁻²)
Voltage (V)
0
20
40
60
0
40
80
120
160
2.2
2.4
2.6
2.8
3.0
(a)
w/o tube
w/ tube
Light intensity (mW·mm⁻²)
Voltage (V)
(b)
Intensity (a.u.)
Wavelength (nm)
0
10 000
20 000
30 000
400
500
600
700
800
470 nm
530 nm
560 nm
650 nm
(c)
w/o tube
2 mm
0
15.0
30.0
Strain (%)
(d)
w/ tube
2 mm
0
15.0
30.0
Strain (%)
(e)
Stress (MPa)
ΔR/R₀ (%)
Strain (%)
0
1
2
3
4
5
0
−5
−10
0
5
10
15
20
25
0%
10 mm
Stretching
25%
10 mm
(f)
w/o tube
3 mm
After 1 min
3 mm
w/ tube
3 mm
After 7 days
3 mm
(g)

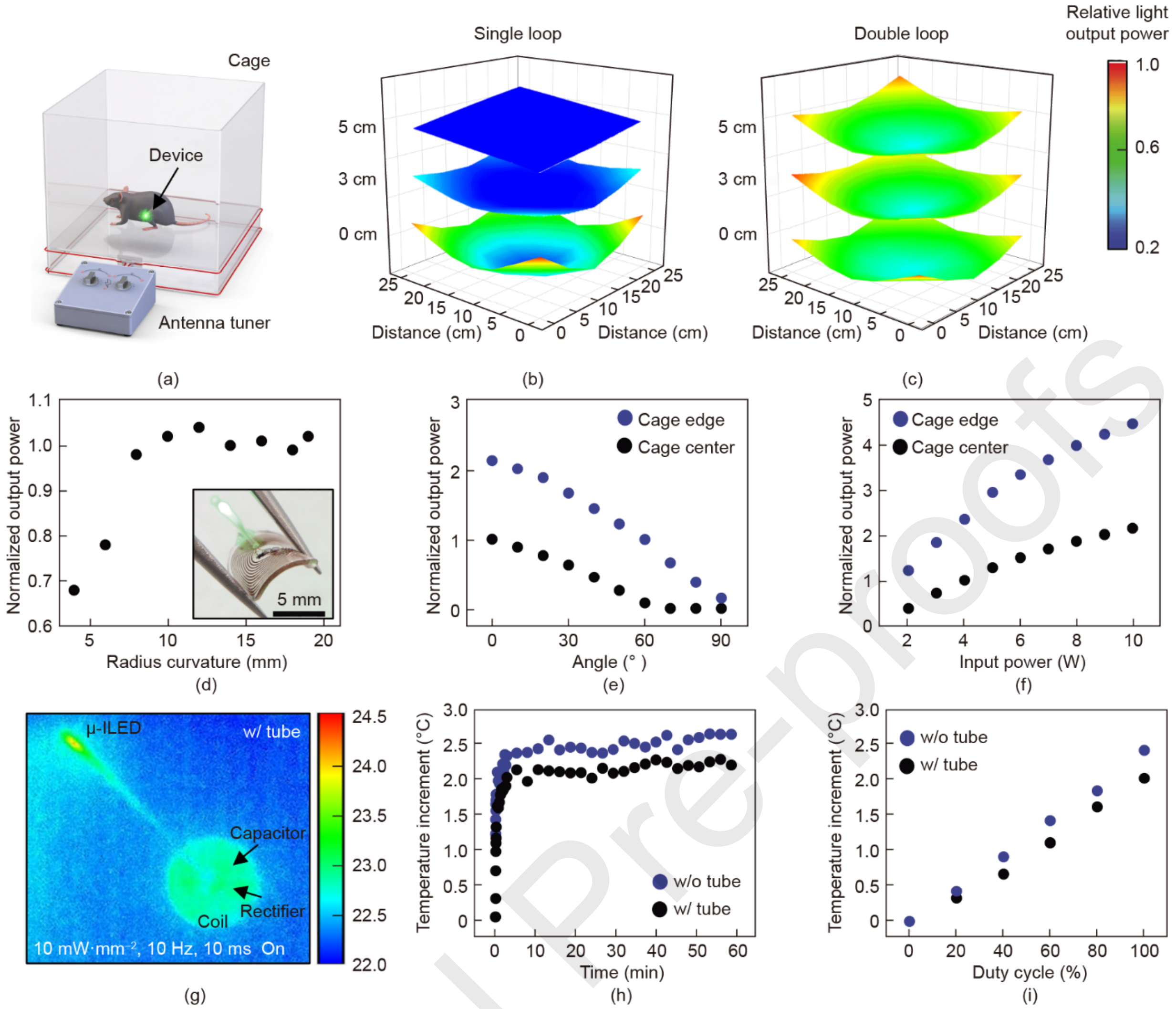
Cage
Device
Antenna tuner
(a)
Single loop
5 cm
3 cm
0 cm
Distance (cm)
Distance (cm)
0 5 10 15 20 25
(b)
Double loop
5 cm
3 cm
0 cm
Distance (cm)
Distance (cm)
(c)
Relative light output power
1.0
0.6
0.2
Normalized output power
Radius curvature (mm)
5 10 15 20
0.6 0.7 0.8 0.9 1.0 1.1
5 mm
(d)
Normalized output power
Angle (°)
0 30 60 90
0 1 2 3
Cage edge
Cage center
(e)
Normalized output power
Input power (W)
2 4 6 8 10
0 1 2 3 4 5
Cage edge
Cage center
(f)
μ-ILED
w/ tube
Capacitor
Rectifier
Coil
10 mW·mm⁻², 10 Hz, 10 ms On
24.5 24.0 23.5 23.0 22.5 22.0
(g)
Temperature increment (°C)
Time (min)
0 10 20 30 40 50 60
0 0.5 1.0 1.5 2.0 2.5 3.0
w/o tube
w/ tube
(h)
Temperature increment (°C)
Duty cycle (%)
0 20 40 60 80 100
0 0.5 1.0 1.5 2.0 2.5 3.0
w/o tube
w/ tube
(i)

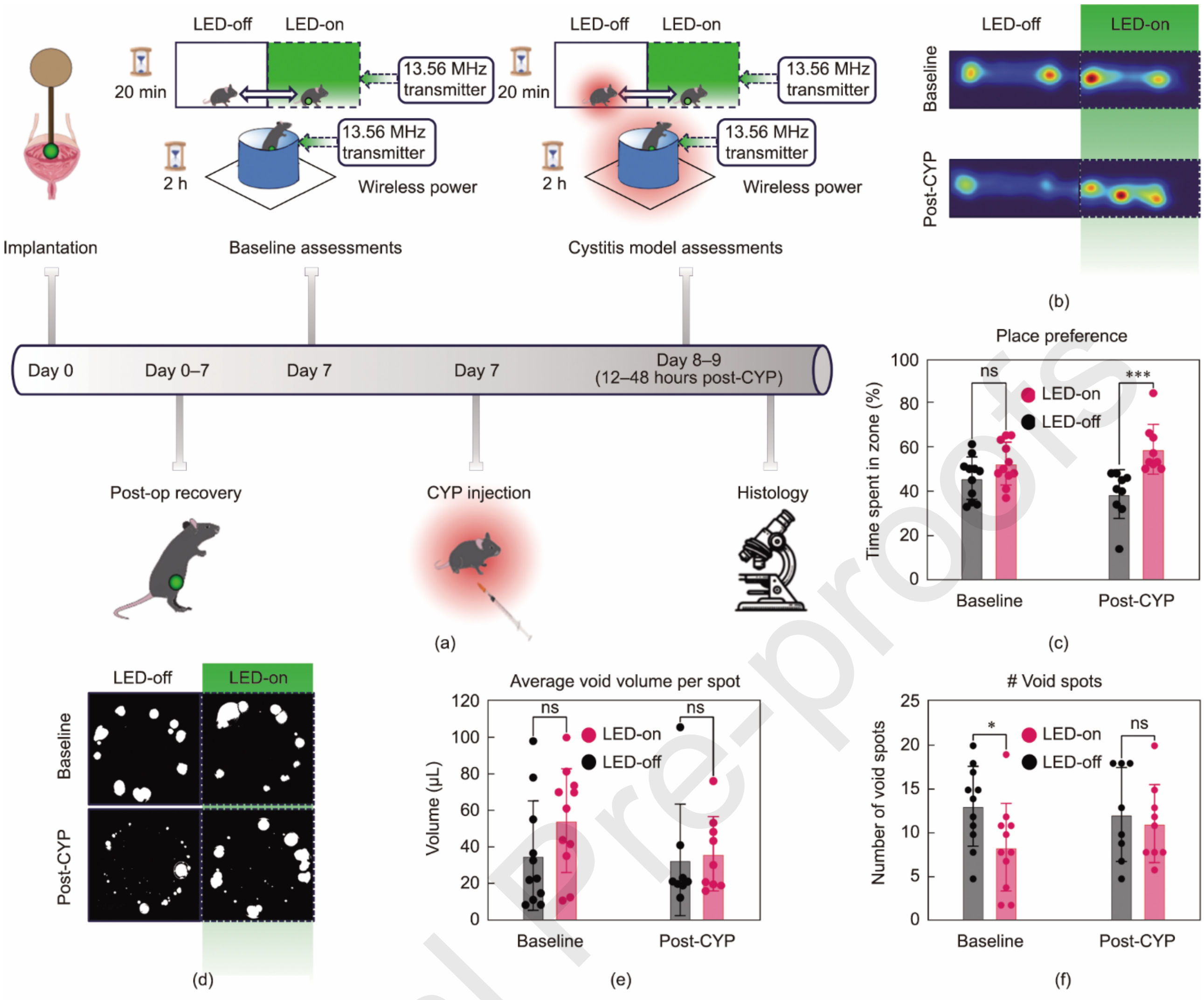
LED-off
LED-on
20 min
13.56 MHz transmitter
2 h
13.56 MHz transmitter
Wireless power
LED-off
LED-on
20 min
13.56 MHz transmitter
2 h
13.56 MHz transmitter
Wireless power
Implantation
Baseline assessments
Cystitis model assessments
Day 0
Day 0–7
Day 7
Day 7
Day 8–9
(12–48 hours post-CYP)
Post-op recovery
CYP injection
Histology
(a)
LED-off
LED-on
Baseline
Post-CYP
(b)
Place preference
Time spent in zone (%)
100
80
60
40
20
0
ns
***
LED-on
LED-off
Baseline
Post-CYP
(c)
LED-off
LED-on
Baseline
Post-CYP
(d)
Average void volume per spot
Volume (μL)
120
100
80
60
40
20
0
ns
ns
LED-on
LED-off
Baseline
Post-CYP
(e)
Void spots
Number of void spots
25
20
15
10
5
0
*
ns
LED-on
LED-off
Baseline
Post-CYP
(f)

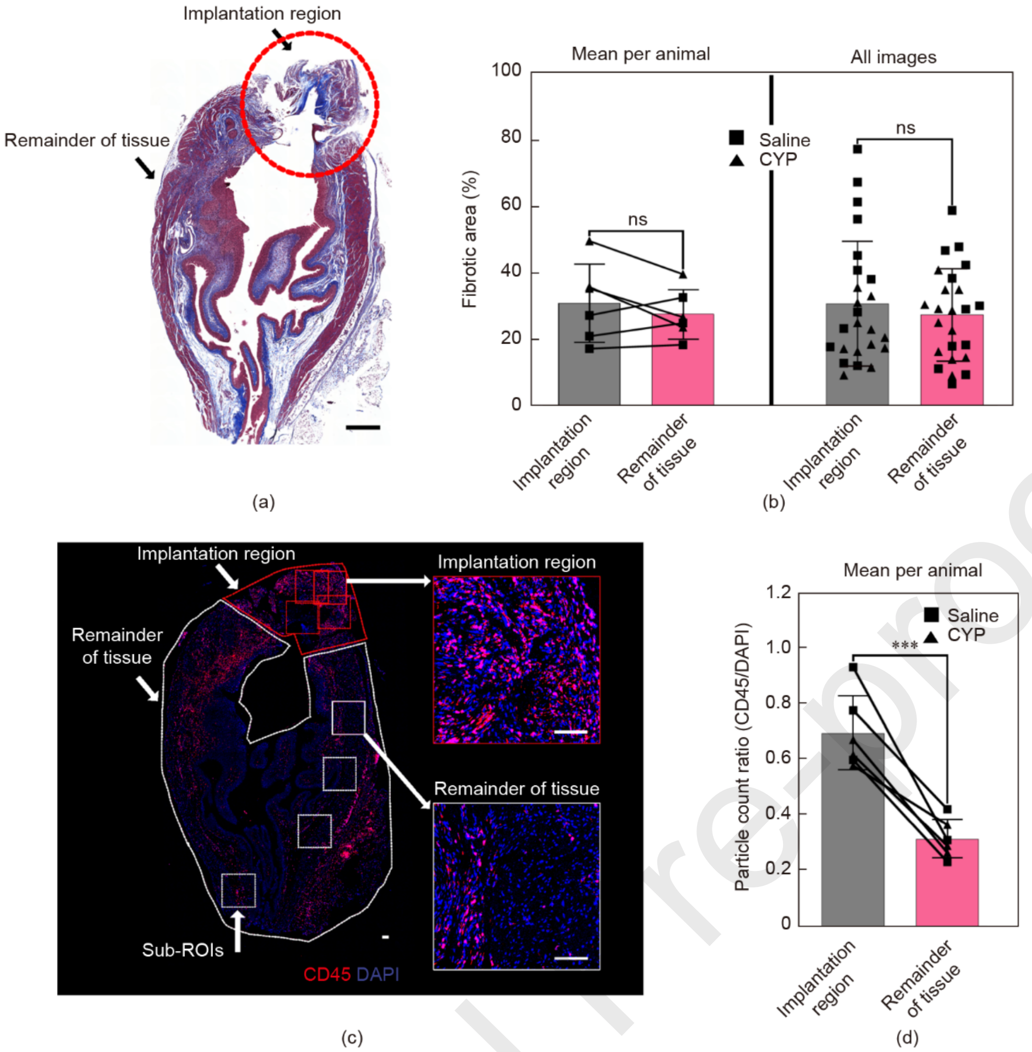
Implantation region
Remainder of tissue
Mean per animal
All images
100
80
60
40
20
0
Fibrotic area (%)
ns
ns
■ Saline
▲ CYP
Implantation region
Remainder of tissue
Implantation region
Remainder of tissue
Implantation region
Remainder of tissue
Implantation region
Remainder of tissue
Sub-ROIs
CD45 DAPI
Mean per animal
1.2
1.0
0.8
0.6
0.4
0.2
0
Particle count ratio (CD45/DAPI)
■ Saline
▲ CYP
***
Implantation region
Remainder of tissue

(a) (b)

(c) (d)